THESIS REPORT

Master's Degree

A Hybrid Actuator

by R. Venkataraman
Advisor: P.S. Krishnaprasad

M.S. 95 -4

Sponsored by
the National Science Foundation
Engineering Research Center Program,
the University of Maryland,
Harvard University,
and Industry

Abstract

Title of Thesis: A HYBRID ACTUATOR

Name of degree candidate: R.Venkataraman

Degree and year: Master of Science, 1995

Thesis directed by: Professor P.S. Krishnaprasad
Department of Electrical Engineering

In this thesis, a new hybrid rotary motor using piezoelectric and magnetostrictive materials is proposed. It is shown that electrically, these materials behave like a capacitor and inductor respectively. The novelty of this motor is the creation of an electrical resonant circuit, whereby the reactive power requirement on the power source is reduced. A simulation program with the elastic effects and a model of impact forces inherent in the design, is written to simulate the behaviour of this motor. The constructional details of a prototype motor which has been built, is then presented. Finally an application of the hybrid actuator to helicopter flaperon actuation is presented as an example of its use.

A HYBRID ACTUATOR

by

R.Venkataraman

Thesis submitted to the Faculty of the Graduate School
of The University of Maryland in partial fulfillment
of the requirements for the degree of
Master of Science
1995

Advisory Committee:

Professor P.S. Krishnaprasad, Chairman/Advisor
Associate Professor W. P. Dayawansa, Co-Advisor
Associate Professor M. A. Austin

Acknowledgements

I thank my advisors Dr. Krishnaprasad and Dr. Dayawansa for giving me the opportunity to work on this wonderful project, and for their patience and understanding during difficult stretches. The discussions I had with them went a long way in clearing my understanding of the problem. My sincere thanks to Mr. Russel Wood and Mr. Mario Garza of the Physics Lab. at the University of Maryland, for bringing to life the concept of the hybrid motor. My friend and colleague Qi Feng Wei has been a great and ready source of help whenever I needed him. Matt Katsuoros– the Automation Specialist at the ISR, has helped me out even during weekends, to make this thesis possible. Last but not least, I thank the Army Research Office which supported this research under Smart Structures URI Contract No. DAAL03-92-G-0121.

Table of Contents

List of Tables

List of Figures

Chapter 1

Introduction

The wide range of materials used by mankind is an indication of his technological advancement. Humans are always in seeking new and better materials which make their life easier, and provide an economic edge over the competition. This can be seen in the use of stone by prehistoric man, and in the invention of bronze, which led to the Bronze Age. The use of iron weapons which were superior to bronze ones marked the beginning of the Iron Age. The modern era, as we know it, began with the discovery of steel, glass, cement etc. . In the beginning of the twentieth century, plastics provided many advantages over metals for many industrial applications and day to day use. Later the use of composite materials, made cars and aircraft lighter and faster. The next step conceivably, would be to make 'SMART' materials that have inherent sensing capability of their environment, and are also able to change the environment (i.e. have actuation capability). Piezoelectric, Electrostrictive and Magnetostrictive materials fit this description.

Rotary motors built using piezoelectric materials are mostly of the Ultrasonic motor type[1]. However, linear motors using the 'inchworm' principle are available commercially[2]. Piezoceramics can be embedded or bonded to beams

for vibration control[3]. Magnetostrictive rotary motors have been developed at NASA, Goddard Space Flight Center[4].

For linear micropositioning, the most common method employed is the use of DC servomotors and stepper motors, with a lead screw for converting the motor's rotary motion to linear motion. Piezoelectric inchworm motors are true linear motors, which have no backlash and extremely high resolution[2].

An electromagnetic d.c motor has a high efficiency but a low torque at a high speed[1]. For low speed, high torque applications, speed reduction gears have to be used which make the system bulky and lower efficiency. Precise positioning would be difficult because of the backlash caused by the gears. Since most high performance electromagnetic motors today are servo type and not steppers, they must use brakes or must keep the power in the hold position. A SMART rotary motor on the other hand, is good for low speed, high torque applications and direct drive is possible because of the high torque. The motors can be made inherently self braking with the power off. Since friction is used to transfer power in most cases, good wear resistant material is needed. Non-frictional mode of power transfer has also been studied([4],[5]).

The magnetostrictive motors tend to be bulky because of the coil, prestress, and biasing arrangements. They deliver more torque but are less efficient. Piezoelectric actuators have the advantage of being miniaturizable and more efficient. Since the SMART actuator (linear or rotary) has features that differ from those of the electromagnetic motor, it can be utilized in areas where the electromagnetic motor is inadequate. For example, the following three applications might be considered.

1. **Flaperon actuation in an helicopter**. A trailing edge flap or a'flaperon'

can provide an active vibration reduction for helicopters[6]. Bimorph actuators (with two piezoceramic sheets) mounted inside the rotor blade have been shown to be feasible for this application([6], [7]). Piezoelectric and electrostrictive stack actuators based on the concept of mechanical amplification can also be used[7]. Magnetostrictive actuators in conjunction with an extension-torsion coupled tube can actuate the twisting motion of a trailing edge flap[8]. The 'hybrid' motor described in this thesis can be used for this application.

2. **Actuators for airplane wing spoilers**. Aerodynamic braking for airplanes is achieved by spoilers in the wings to provide increased drag resistance. The actuators controlling these spoilers are hydraulic. SMART actuators can be used instead, making the airplane lighter.

3. **Focusing mechanisms in cameras**. Previously, a d.c motor had to be installed in the main body and used a transmission system, including speed reduction gears, to drive the lens[1]. With the ring-type ultrasonic motor, no transmission is needed and a response time of a few milliseconds is realized, which compares favourably with the time of 100ms for the former focusing mechanism. In addition, there is advantage of silence due to the direct drive.

We see that previous research has focused on actuators with magnetostrictive or piezoelectric materials, but never using a combination of both. The main idea of this thesis is to build a 'hybrid' actuator taking advantage of the properties of both SMART materials. **Electrically, as piezoelectric actuators are essentially capacitive in nature while magnetostrictive actuators are**

inductive, an electrical resonance can be created which would reduce the reactive power load on the power source.

In Chapter 2, we study the basic properties of the materials, and derive linear ODE's to describe their behaviour. A simulation feasibility study was done, and this is the content of Chapter 3. The hybrid motor is unidirectional, since we use a resonant circuit to drive it. The drive circuit modification for bidirectional motion and an application example to helicopter flaperon actuation make up Chapter 4. The details of construction for a prototype hybrid actuator are presented in Chapter 5. Conclusions and directions for future work are the purpose of the last chapter.

Chapter 2

Smart Materials

The stress-strain characteristic of 'SMART' materials can be controlled by the application of external factors like heat, electric or magnetic fields. This property makes the materials 'SMART'. Magnetostrictive materials are those whose characteristic can be controlled using magnetic fields, while piezoelectric materials are those which are affected by electric fields.

Magnetostrictive materials are solids which typically develop large mechanical deformations when subjected to an external magnetic field. The magnetostrictive effect was first discovered in nickel by James Joule in 1840. Cobalt, iron and alloys of these materials were later found to show significant magnetostriction effects; however, the strains were still limited to 50 ppm as in nickel. Researchers at the Naval Ordnance Laboratory discovered the extraordinary magnetostrictive behaviour of the Terbium-Iron alloy. Terfenol-D is a commercially available magnetostrictive material which incorporates the rare-earth element dysprosium. This material offers strains upto 2000 ppm which is an order of magnitude superior to the current generation of piezoceramic materials.

Piezoelectricity is a word derived from the Greek word '*piezein*' for '*press*'. The term first appeared in the scientific literature in 1880 when Pierre and Paul-

Jacques Curie published a paper, describing how various crystals developed an electric charge on their surface when they were mechanically deformed in certain directions. Their work focused upon crystals of tourmaline, Rochelle salt and quartz. One year later, they discovered the converse effect whereby these crystals changed their shape when they were subjected to an electric field.

This piezoelectric phenomenon is similar to electrostriction, which is a property of all dielectrics. The electrostriction phenomenon is evidenced in practice as a small change of geometry of a body when it is subjected to an electric field. The direction of this small change in geometry does not change if the direction of electrical field is reversed. In sharp contrast to this situation, piezoelectric materials, exhibit a reversal in the direction of geometrical change when the direction of the electrical field is reversed [9].

2.1 Magnetostriction

Magnetostriction is a result of the rotation of small magnetic domains which causes internal strains in the material [10]. These strains result in a positive expansion of the magnetostrictive rod in the direction of a magnetic field. As the field is increased more domains rotate and become aligned until finally saturation is achieved, where nearly all domains are aligned in the direction of the field. If the field is reversed the domains reverse direction but again align along the field direction and also result in a length increase. Thus, the negative cycle of a current oscillation produces a positive expansion just as in the case of a positive current cycle. Figure 2.1 shows the strain vs H characteristic for $Tb_{.27}Dy_{.73}Fe_{1.90}$, commercially known as Terfenol-D[10].

In the linear region the transduction may be described by the fundamental

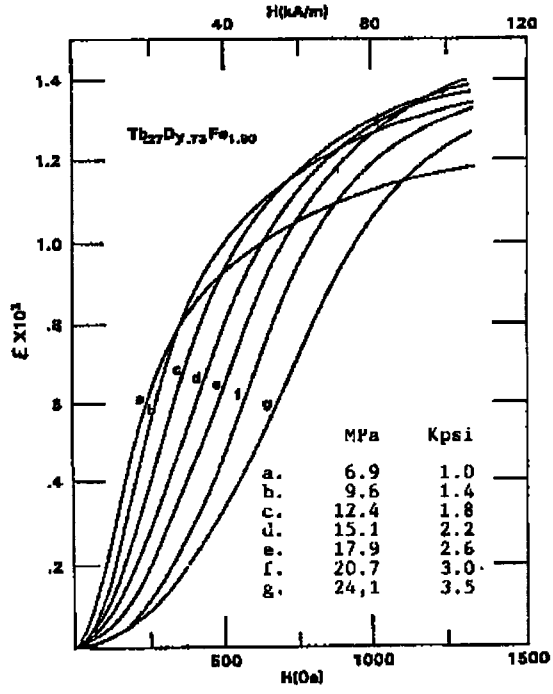

Figure 2.1: Approximate strain vs magnetic field intensity curves for compressed ETREMA Terfenol-D .

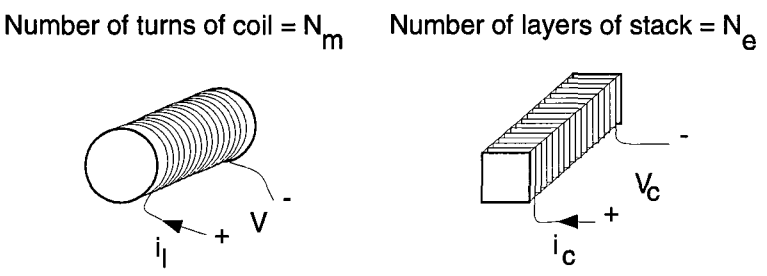

Figure 2.2: The magnetostrictive rod and the electrostrictive stack.

equation set

$$\delta = s^h \sigma + d_m H \tag{2.1}$$

$$B = d_m \sigma + \mu_T H \tag{2.2}$$

where δ is the strain, σ is the mechanical stress,H is the magnetic field intensity and B is the flux density. We assume the vector quantities are directed along the axis of the rod. The magnetostrictive constant d_m corresponds to the slope of the linear region of the $\delta - H$ curve, while the free permeability μ_T corresponds to the slope of the $B - H$ curve in the first quadrant.

2.1.1 Derivation of Voltage - Current - displacement relations for a thin magnetostrictive rod

Consider a thin magnetostrictive rod as shown in figure 2.3. As the cross-sectional area is very small compared to its length , we can assume that the B field inside is pointing in the x-direction, and the mechanical stress is uniform in the same direction. Edge effects are neglected. The operating region is also assumed to lie within the linear region for the material. Hence,

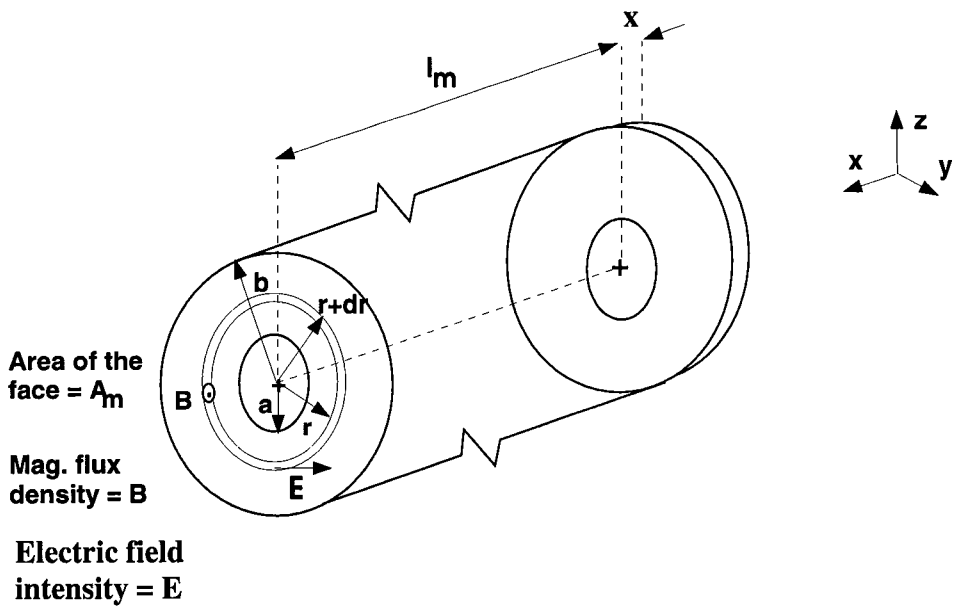

Figure 2.3: Derivation of V-I-x relationship for the thin magnetostrictive rod.

$$\sigma = \frac{P}{A_m} \tag{2.3}$$

$$H = \frac{N_m I_l}{l_m} \tag{2.4}$$

$$x = \delta l_m \tag{2.5}$$

where, P is the longitudinal force applied, N_m is the number of turns of coil wrapped around the rod and I_l is the electric current through the coil. The quantities A_m & l_m are the area of the face of the rod and its length respectively. x is the net change in length of the rod due to the application of the force P and the current I_l. If ϕ is the magnetic flux through the rod and V_m is the voltage across the ideal coil then,

$$V_m = N_m \dot{\phi} \tag{2.6}$$

$$\phi = BA_m \tag{2.7}$$

Equations 2.1- 2.2 and 2.3 through 2.7 yield the following equation,

$$V = \frac{d_m N_m A_m \dot{x}}{s^h l_m} + \frac{\mu^T N_m^2 A_m}{l_m} \left(1 - \frac{d_m^2}{s^H \mu^T}\right) \dot{I}_l \tag{2.8}$$

This is the basic relationship that is obeyed by the voltage, current and the strain for an ideal magnetostrictive rod. Eqn. 2.8 can be written as,

$$V = C\,\dot{x} + L_f\,(1 - k^2)\dot{I}_l \tag{2.9}$$

In equation 2.9, L_f is the free inductance of the rod (i.e., the inductance with no applied force). The coupling coefficient k is an important figure of merit for a transducer. For ETREMA Terfenol - D the value ≈ 0.72 which is comparable to the lead zirconate titanate piezoelectric ceramic material [10]. The square of the coupling coefficient is equal to the ratio of the energy converted to the total energy stored. For $k = 0.7071, k^2 = 0.5$ and 50% of the total electrical energy stored is converted into mechanical energy.

The high frequency limitation of the magnetostrictive rod is generally due to eddy current losses. In our derivation, we have also assumed the coil to have zero resistance. We now assume a non-zero coil resistance, take the eddy currents into account, and derive equations for a non-ideal magnetostrictive rod [11].

Let the resistivity of the magnetostrictive material be ρ, and the resistance of the coil be R. The flux density B is along the x-direction (figure 2.3) and the

electric field E in the material lies in the y-z plane with no radial component. Then,

$$|E_\phi| = \frac{|\dot{B}|\, r}{2} \tag{2.10}$$

$$|J| = \frac{|E|}{\rho} = \frac{|\dot{B}|\, r}{2\,\rho} \tag{2.11}$$

Therefore the current in an element of thickness dr and length l_m is

$$di = \frac{|\dot{B}|\, r\, l_m\, dr}{2\,\rho} \tag{2.12}$$

The voltage at a point on the element can be found from a contour integral around the element, and it is

$$V(r) = |E_\phi|\, 2\,\pi\, r = |\dot{B}|\, \pi\, r^2 \tag{2.13}$$

The Power lost due to the eddy currents in the element is

$$dP(r) = V(r)\, di = \frac{|\dot{B}|^2\, \pi\, l_m\, r^3\, dr}{2\,\rho} \tag{2.14}$$

The total instantaneous power lost due to the eddy currents,

$$P = \int_a^b dP(r) = \frac{(V_m - I\,R)^2\, l_m}{N^2\, 8\pi\rho}\, \frac{b^2 + a^2}{b^2 - a^2} \tag{2.15}$$

Therefore the resistance seen by the eddy current (figure 2.4)

$$R_{ed} = \frac{N^2\, 8\pi\rho}{l_m}\, \frac{b^2 - a^2}{b^2 + a^2} \tag{2.16}$$

Expressing V_m in terms of I_l we get,

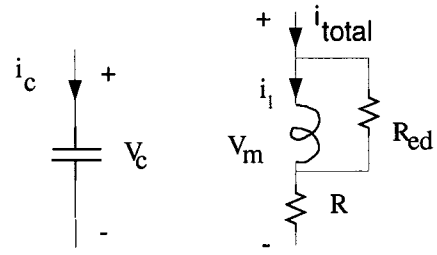

Figure 2.4: Electrical equivalents of the thin Electrostrictive stack and the thin magnetostrictive rod.

$$V_m = \left(\frac{d_m A_m N_m \dot{x}}{s^h l_m} + \frac{\mu^T N_m^2 A_m}{l_m} \left(1 - \frac{d_m^2}{s^H \mu^T} \right) \dot{I}_l \right) \left(1 + \frac{R}{R_{ed}} \right) + I_l R \qquad (2.17)$$

2.2 Piezostriction

The piezoelectric phenomenon is similar to electrostriction, which is a property of all dielectrics. For a piezoelectric phenomenon to occur in a material, the crystal lattice should have no center of symmetry. By applying mechanical deformations to these crystals, electric dipoles are generated and a potential difference develops that is contingent upon the changing deformations. Therefore, typical and practical uses are in situations involving dynamical strains of an oscillatory nature [12].

Modified lead zirconate titanate (PZT) based ceramics are currently the leading materials for piezoelectric applications. The Strain vs. Electric field curve is shown in figure 2.5.

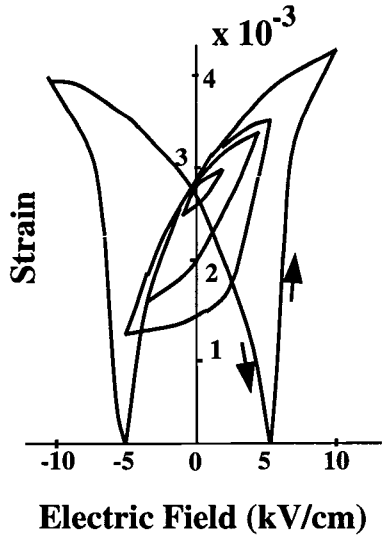

Figure 2.5: Strain vs Electric Field for a Piezoelectric material

2.2.1 Derivation of Voltage - Current - displacement relations for a thin piezoelectric stack

A typical piezoelectric stack is shown in figure 2.2. The transduction in the linear region may be described by [9],

$$\delta = s^e \sigma + d_e E \tag{2.18}$$

$$D = d_e \sigma + \epsilon E \tag{2.19}$$

where δ is the strain, E is the Electric field intensity and D is the Electric Displacement vector. The mechanical stress is σ. Again we assume the vector quantities are directed along the axis of the stack. Also, the electrostrictive constant d_e corresponds to the slope of the linear region of the δ - E curve , while the free permittivity constant ϵ corresponds to the slope of the curve in the first quadrant of the D - E curve. s^e is the inverse of the Young's modulus

for the material. [13] gives an experimental method for modeling the Young's modulus as a complex quantity, thus including losses into the model.

We note that the equations are analogous to the ones for the magnetostrictive material. So, by following the derivation of equation 2.8 for the ideal magnetostrictive rod we obtain,

$$I_c = \frac{d_e A_e N_e \dot{y}}{s^e l_e} + \frac{\epsilon N_e^2 A_e}{l_e}\left(1 - \frac{d_e^2}{s^e \epsilon}\right)\dot{V}_c \tag{2.20}$$

where, I_c is the current through the electrostrictive stack.

Chapter 3

The Hybrid Actuator

The basic scheme of the proposed actuator is shown in figure 3.1. The piezoelectric stack clamps the mass m to the disc while the magnetostrictive rod pushes the mass tangential to the disc. As the angular displacement of a disc of radius 5 cm in one such push is of the order of 10^{-4} radians, we can achieve an appreciable displacement per second by operating at sufficiently high frequency. We can use another magnetostrictive rod as shown in figure 3.2 to achieve bi-directional motion. In figure 3.2, rod 2 contracts in length when rod 1 expands and vice versa. In the following discussion the origin of the lab. frame of reference is the edge of the disc at power off (Point P in figure 3.2).

The electrical connection of the actuator elements is shown in figure 3.3.

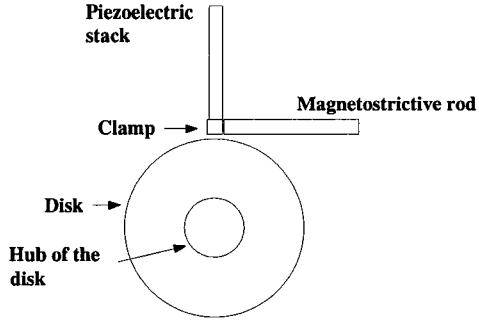

Figure 3.1: Basic scheme for an unidirectional hybrid actuator.

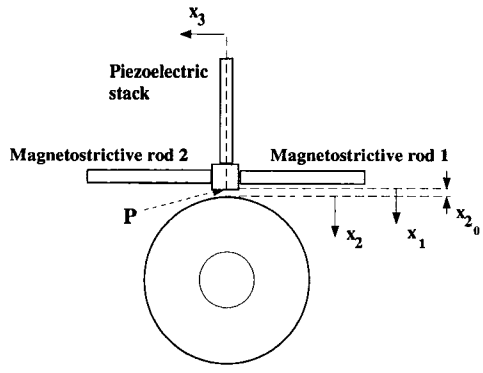

Figure 3.2: Schematic diagram of the actuator.

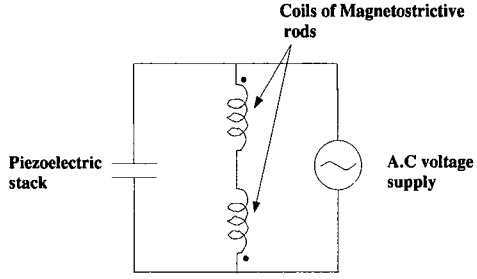

Figure 3.3: Electrical connection.

Both the magnetostrictive rods have an identical permanent magnet bias. But their coils are connected such that the current adds to the flux for one rod(which elongates), while it subtracts for the other (which contracts). This achieves motion of the disc in one direction. If the coil connections are reversed then we can achieve motion in the other direction.

During one cycle of the applied voltage, the actuator has two distinct phases of operation.

1. The piezostrictive stack and the clamp unit are in 'good contact' (i.e clamped) with the disc.

2. The piezostrictive stack and the clamp unit are not in 'good contact' with

(i.e separate from) the disc.

Definition 3.0.1 *Good contact has been made if the force between the clamp and the disc is greater than zero.*

The disc is an elastic body and it undergoes deformation as the clamp presses into it. Hence, a good model for the disc is needed, before a simulation of the actuator can be done. As an approximation, a mass-spring model of the disc can obtained by doing a finite element analysis. Using PATRAN, a stress analysis was done to obtain the strain energy and the max. displacement of the tip of the disc, for a unit stress. Figure 3.4 is an output of the PATRAN program, and it shows the stress distribution in the disc. If we replace the disc to by an equivalent mass-spring system, then the mass should be displaced by the same amount as the tip of the disc. Also, the strain energy in the disc is now stored in the equivalent spring. Therefore, equation 3.1 gives the stiffness of the spring.

$$StrainEnergy = \frac{1}{2} K_{eff}\, x^2 \tag{3.1}$$

We now do a modal analysis of the disc using PATRAN, and assume the lowest resonant frequency to be the resonant frequency of the spring-mass system. Equation 3.2 then gives the mass of the system. Table 3.1 gives the equivalent mass and the spring constant for different parameters of the disc.

$$Resonance frequency = \sqrt{\frac{K_{eff}}{M_{eff}}} \tag{3.2}$$

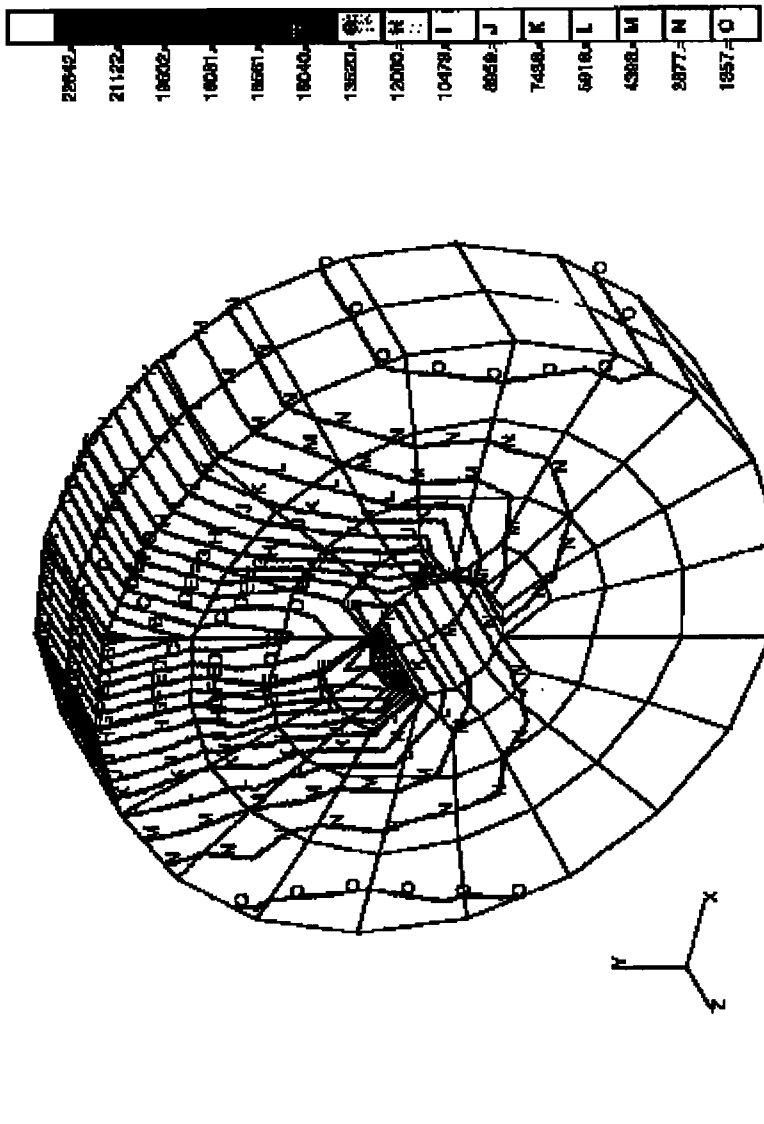

Figure 3.4: A typical stress distribution in a disc.

Disc radius (cm)	*Hub radius (cm)*	*Disc thickness (cm)*	*Equivalent mass (kg)*	*Equivalent* spring *(N/m)*
5.0	1.0	1.0	1.044	7.945e8
7.0	1.0	1.0	4.7957	7.7246e8
7.0	2.0	1.0	2.1382	8.3787e8
5.0	2.0	1.0	0.3184	8.8018e8
4.0	1.0	1.0	0.3407	8.128e8

Table 3.1: Equivalent mass-spring values for the disc.

3.1 Clamped condition

When the clamp and the disc are clamped together (i.e they are in 'good contact'), the following set of equations fully describes the system.

$$I\ddot{\theta} + b\dot{\theta} + T_{load} = \pm\mu F r \tag{3.3}$$

Here I is the moment of inertia of the disc about its axis, b is the damping coefficient, T_{load} is the load torque, μ is the coefficient of dynamic friction, F is the normal force on the disc due to the clamping action and r is the radius of the disc. The $\pm$ sign shows that the direction of the frictional force may aid the motion of the disk at a given instant of time or it may oppose it. The transduction property of the magnetostrictive actuator is given by equation 2.17 which can be rewritten as,

$$\dot{I}_l = -\frac{d_m \dot{x}_3}{N_m(s^h \mu^T - d_m^2)} - \frac{R i_l}{k_1} - \frac{V_a + V_c}{k_1} \tag{3.4}$$

The clamping operation can be described by the equations

$$M_1 \ddot{x}_1 + K_1 x_1 = -F + C_1 V_c \tag{3.5}$$

$$M_2 \ddot{x}_2 + K_2 (x_2 - x_{2_0}) = F \tag{3.6}$$

where

M_1 =*Mass of the Piezo stack + Mass of the clamp*

K_1 =*Stiffness of the Piezo stack and the clamp in series* $= \frac{\frac{A_e}{s^e l_e} \frac{A_{clamp}}{s^{bronze} l_{clamp}}}{\frac{A_e}{s^e l_e} + \frac{A_{clamp}}{s^{bronze} l_{clamp}}}$

$C_1 = \frac{d_e A_e N_e}{s^e l_e}$

M_2 =*Equivalent mass of the disk.*

K_2 =*Equivalent stiffness of the disk.*

F = *The clamping force.*

V_c =*Voltage on the Piezo-stack.*

x_{2_0} =*Initial separation of the disc and clamp surfaces.*

x_2 =*The position of the edge of the disc w.r.t the lab. frame.*

x_1 =*The position of the edge of the clamp w.r.t the lab. frame.*

It must be mentioned here that equation 3.5 is an approximation of the actual system as shown in figure 3.5. In figure 3.5, x_1, x_2, x_4 are the co-ordinates of the point masses M_{clamp},M_{disc}, M_{piezo} respectively with respect to the lab. frame of reference. Figures 3.6, 3.7 show the bode plots of the two systems in figure 3.5. As the bode plots are identical below $3 * 10^4 rad/s$ and the extra poles in figure 3.7 occur at a much higher frequency than the one we are interested (1 Khz),

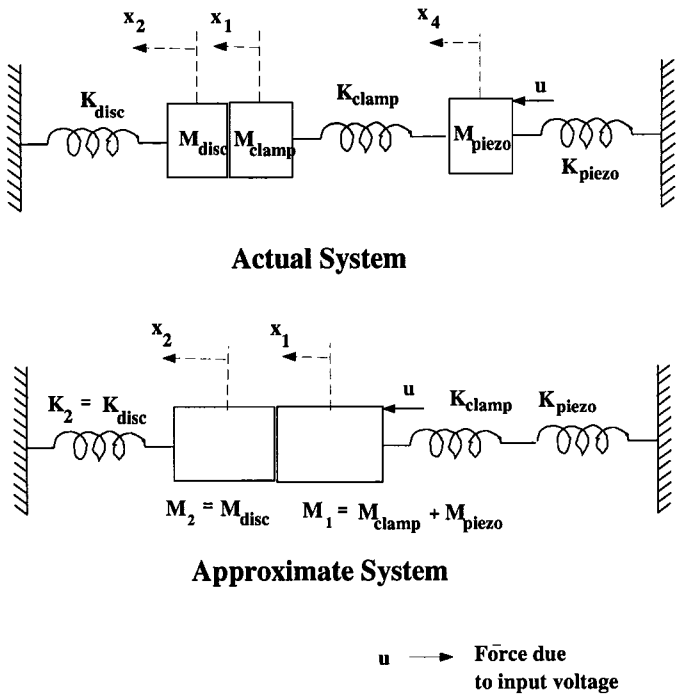

Figure 3.5: Approximation of the stack, clamp system.

we are justified in making the approximation. This reduces the computations involved in simulating the actuator. Henceforth the term clamp or the stack will mean the clamp plus the stack system (the approximate system).

The motion of the clamp tangential to the disc can be described by

$$M_3\,\ddot{x} + K_3\,x = \pm\,\mu\,F\,r + C_2\,I_m \tag{3.7}$$

where

M_3 =*Mass of the magnetostrictive rod + Mass of clamp.*

K_3 =*Stiffness of the magnetostrictive rod.*

$$C_2 = \frac{d_m\,A_m\,N_m}{s^m\,l_m}$$

I_m =*The current through the coil of the magnetostrictive rod*

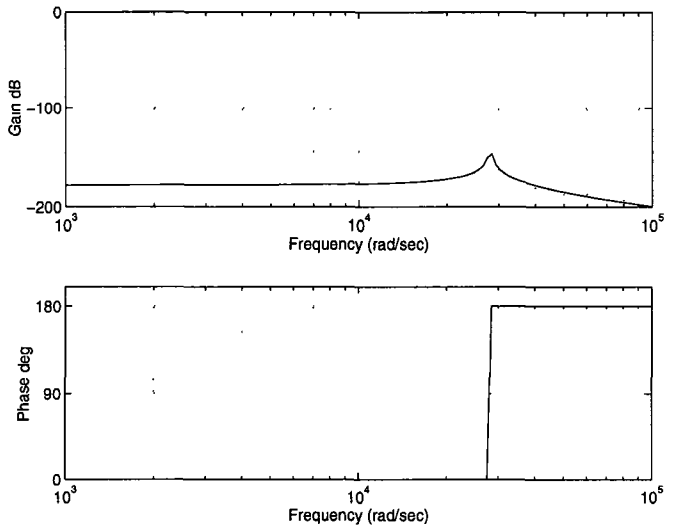

Figure 3.6: Bode plot of the approximate system.

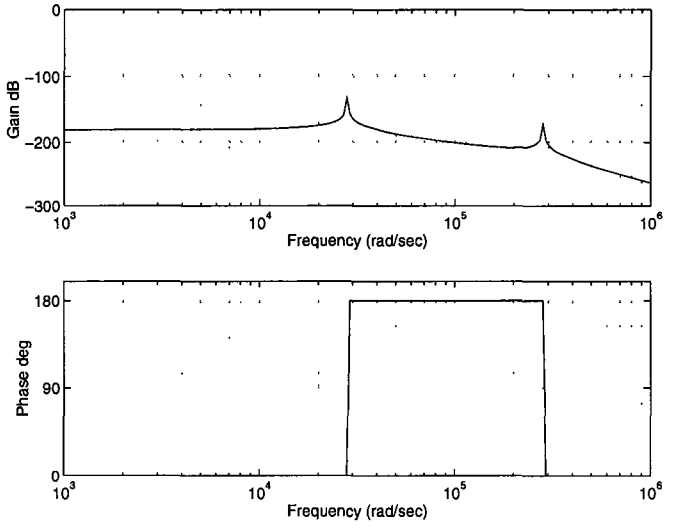

Figure 3.7: Bode plot of the actual system.

r = *Radius of the disk.*

F = *Normal force of contact between the clamp and the disc.*

μ =*Coefficient of friction of the clamp and disc surfaces.*

The sign of the frictional force depends on the relative velocities of the clamp and the edge of the disk when they come into contact.

Equation 3.7 describes the behaviour of the pushing magnetostrictive actuator in both half-cycles. The other actuator is contracting freely and hence its behaviour can be described by equation 3.7 with $F = 0$. But its effect appears in the circuit equation which is,

$$V_a = V_c = 2 * V_m \tag{3.8}$$

where,

V_c =*Voltage of the piezoelectric stack*

V_m =*Induced voltage of the coil + Voltage across the coil resistance.*

V_a =*Amplifier Voltage*

To completely describe the entire system, we need one more equation which is,

$$x_1 = x_2 \tag{3.9}$$

This equation says that the clamp and the disc edges move together. Equations 3.5, 3.6 and 3.9 then yield a state equation for the force of contact.

$$\dot{F} = \frac{M_1 M_2}{M_1 + M_2} \left(\left(\frac{K_2}{M_2} - \frac{K_1}{M_1} \right) + \frac{C_1 \dot{V}_a}{M_1} \right) \tag{3.10}$$

3.2 Unclamped Condition

All the equations of the previous section hold (with $F = 0$) except eqn. 3.9 .

3.3 Transition from Unclamped to Clamped state

As the piezoelectric stack increases in length, the clamp moves toward the disc and impacts with it. The impact force depends on the effective masses of the disk and the clamp, the velocities of the disk and the clamp edges, and the voltage on the stack. It is critical to know what the value of this force is as the brittle ceramic might not be able to withstand it. Recently a new algorithm for computing the impact force appeared in [14]. The solution methodology assumes that the Hertz law on impact is valid.

The disc and the clamp system is considered to be spring-mass system as shown in fig 3.8. The Hertz law of impact says that,

$$\alpha = K\left[f\left(t\right)\right]^{2/3} \tag{3.11}$$

where α is the relative approach of the striking body, $f\left(t\right)$ is the contact force and K is the Hertz constant[14], which is determined by the local geometry and material properties of the impacting objects. The relative approach is the difference between the displacement of the disc and the clamp, measured from the instant of initial contact. Hence,

$$\alpha = x_1(t) - x_2(t) \tag{3.12}$$

where $x_2(t)$ is displacement of the disc at the point of contact, $x_1(t)$ is the displacement of the clamp under the contact force $f(t)$.

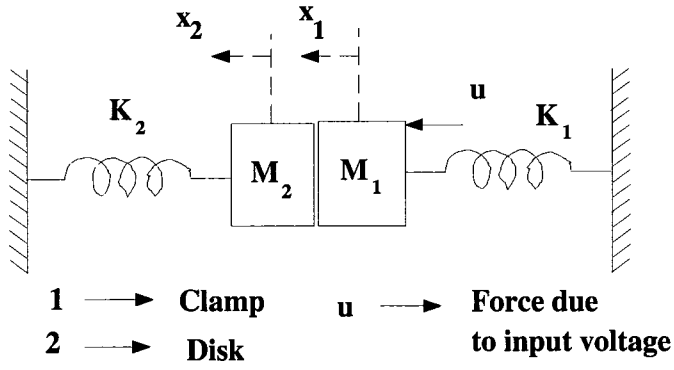

Figure 3.8: Impact force calculation.

If V is the voltage of the piezoelectric stack at the time of impact, and ω_0 is the frequency of the voltage variation (assumed sinusoidal), then

$$x_1(t) = \frac{v_{clamp}\, sin(\omega_{clamp} t)}{\omega_{clamp}} - \frac{1}{\omega_{clamp}\, m_{clamp}} \int_0^t f(\tau)\, sin[\omega_{clamp}(t-\tau)]\, d\tau$$

$$+\frac{C_1 V_{max}}{m_{clamp}\,(\omega_{clamp}^2 - \omega_0^2)} \left(sin(\phi_0) \sqrt{1 + \frac{\omega_{clamp}^2}{tan^2(\phi_1)}}\, sin(\omega_{clamp} t + \phi_1) \right.$$

$$\left. +\frac{sin(\omega_0 t + \phi_0)}{1} \right) \tag{3.13}$$

where,

$$C_1 = \frac{d_e\, A_e\, N_e}{s^e\, l_e}$$

The constants ϕ_0, ϕ_1 are given by the equations,

$$\phi_0 = sin^{-1} \frac{V}{V_{max}} \tag{3.14}$$

$$\phi_1 = tan^{-1} \left(\frac{\omega_{clamp}}{\omega_0}\, tan(\phi_0) \right) \tag{3.15}$$

while $x_2(t)$ is given by,

$$x_2(t) = \frac{v_{disc}\, sin(\omega_{disc} t)}{\omega_{disc}} + \frac{1}{\omega_{disc}\, m_{disc}} \int_0^t f(\tau)\, sin[\omega_{disc}(t-\tau)]\, d\tau \tag{3.16}$$

The resonant frequencies are given by the equations,

$$\omega_{clamp} = \sqrt{\frac{k_{clamp}}{m_{clamp}}} \tag{3.17}$$

$$\omega_{disc} = \sqrt{\frac{k_{disc}}{m_{disc}}} \tag{3.18}$$

and v_{clamp}, v_{disc} are the initial velocities of the clamp and the disc. The calculation of K is detailed in [14],

$$\lambda = \frac{1 - \nu_{steel}^2}{E_{steel}\,\pi}$$

$$p = \frac{4\sqrt{r_{disc}}}{6\,\pi\,\lambda}$$

$$K = (1/p)^{2/3} \tag{3.19}$$

where ν_{steel} is the poisson's ratio for steel and E_{steel} is the Young's Modulus for steel.

Equations 3.11 through 3.16 give,

$$f(t) = \left(\frac{1}{K}\left(a(t) - \frac{1}{\omega_{clamp}\,m_{clamp}}\int_0^t f(\tau)\,sin[\omega_{clamp}(t-\tau)]\,d\tau\right.\right.$$

$$\left.\left. - \frac{1}{\omega_{disc}\,m_{disc}}\int_0^t f(\tau)\,sin[\omega_{disc}(t-\tau)]\,d\tau\right)\right)^{3/2} \tag{3.20}$$

where,

$$a(t) = \frac{v_{clamp}\,sin(\omega_{clamp}t)}{\omega_{clamp}} - \frac{v_{disc}\,sin(\omega_{disc}t)}{\omega_{disc}}$$

$$+\frac{C_1 V_{max}}{m_{clamp}\,(\omega_{clamp}^2 - \omega_0^2)}\left(sin(\phi_0)\sqrt{1 + \frac{\omega_{clamp}^2}{tan^2(\phi_1)}}sin(\omega_{clamp}t + \phi_1)\right.$$

$$+\frac{sin(\omega_0 t + \phi_0)}{1}\Bigg) \tag{3.21}$$

Equation 3.3 has a unique solution and the solution can be found using Picard iteration [15].

By simulation it was found that the time of impact was much smaller than the time-interval of contact. If we make the approximation that the input voltage remains constant during the impact duration, then impact force obtained approximates the actual force very well and is estimated faster because of the simpler expression for the impact force.

It must be noted that the impact model used is conservative since there is no loss of energy. Hence we restrict the number of impacts to one and assume the second collision to be a perfectly inelastic one. Hence after the second collision, we have

$$v_{disc_{after}} = v_{clamp_{after}} = \frac{m_{clamp_{before}} v_{clamp_{before}} + m_{disc_{before}} v_{disc_{before}}}{v_{clamp_{before}} + v_{disc_{before}}} \tag{3.22}$$

3.4 Transition from Clamped to Unclamped state

The force of contact between the clamp and the disk in the clamped state is greater than zero. When this force reduces to zero, 'good contact' is lost.

The algorithm for the simulation is in figure 3.9.

3.5 Friction

The selection of frictional materials is very important, in order to prevent damage to the face of the clamp and the disk, and the occurrence of unwanted noise, as

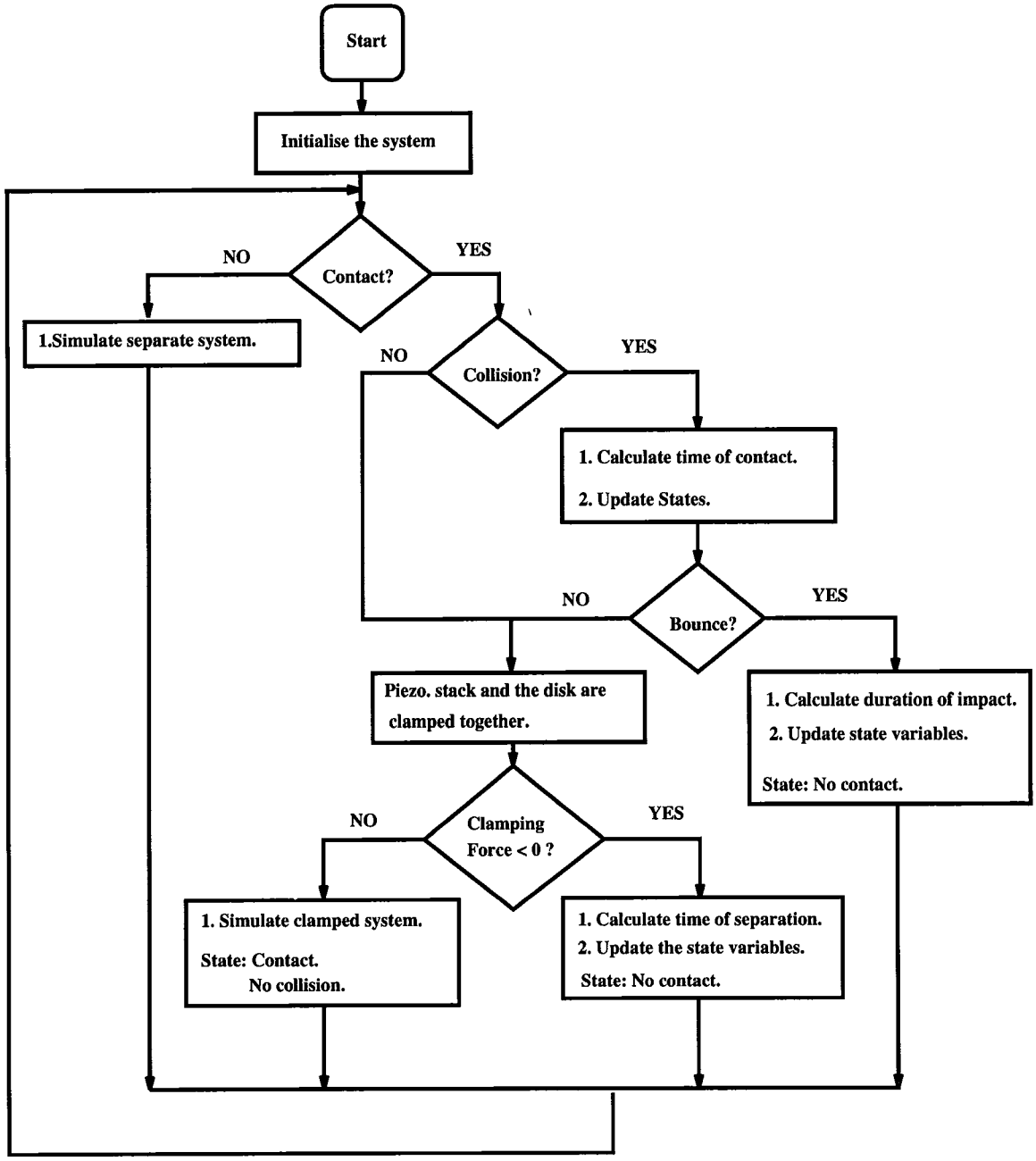

Figure 3.9: Algorithm for computer simulation.

well as to improve the efficiency of energy conversion of the actuator.

The modeling of the friction phenomenon is very complicated [16]. It is a function of the materials in contact, the surface roughness, the relative velocity of the bodies at the junction and the normal force. The frictional force is discontinuous at zero velocity because of static friction. An integrated friction model comprises of four velocity regimes, two time dependent properties and several mechanism dependent properties for constant normal force [16].

1. The four velocity regimes:

   Static friction Displacement is proportional to force.

   Boundary lubrication Friction is dependent on surface properties and lubricant chemistry.

   Partial fluid lubrication If static friction is greater than Coulomb friction, friction decreases with increasing velocity.

   Full fluid lubrication Friction is function of velocity.

2. The two time dependent properties:

   Rising static friction The static friction rises with increasing dwell time.

   Frictional memory In partial fluid lubrication, friction varies with velocity and load; a change in friction will lag changes in velocity or load.

A model for the variation of the frictional force with changes in the normal force can be found in [17]. What all this amounts to, is that an accurate friction model which accounts for all the effects precisely is out of question. For our purposes, the following friction model is used in the simulation.

$$F = \mu N \tag{3.23}$$

where, F = *Frictional force,*

μ = *Coefficient of friction,*

N = *Normal force.*

On the other hand, a lot of experimental studies on frictional materials applicable to ultrasonic motors have been undertaken in Japan [1]. One of the studies concluded that the features required in a frictional material were as follows [18]. A certain amount of defacement is allowable, as long as each particle dislodged is small and significant recombination of the particles does not readily occur; in addition, the dislodged particles must be easily eliminated from the motor. Frictional material that suffers breakage of large particles by friction is not suitable for an ultrasonic motor. Large dislodged particles and portions where the compound is broken away, are deemed to prevent effective conversion of vibrational energy from the stator vibrator to the rotor.

Also, it has been shown experimentally that lubrication of the contact interface between the rotor and the stator is an interesting solution for improving the performance of an ultrasonic motor [1].

3.6 Simulation results

It is first essential to choose the parameters of the system (i.e the sizes of the components). Since we are interested in showing proof of concept by designing the prototype, the size of the actuator is not a concern. Consequently, we can choose commercially available components so that the cost of the prototype is

low. Tables 3.2 and 3.3 list the parameters chosen and the various physical constants of the actuator system.

To get an idea of the resonant frequencies of the system, we assume the clamp to be permanently connected to the disc, and then we look at the bode plots of this linear system. Figure 3.10 shows the bode plots of the angular velocity and the displacements of the edges of the magnetostrictive rod and the clamp respectively. The input is the amplifier voltage. It can be seen that the resonant frequencies for all three transfer functions coincide at about 4500 Hz. It can also be seen that the resonance peaks are quite short and that the magnitude at 1000 Hz is comparable to the resonant peak. But if we look at the equation for the impact force (eqn. 3.3), we see that the impact force is inversely propotional to $\omega_{clamp}^2 - \omega_0^2$. This suggests that we cannot make the amplifier frequency equal to the resonant frequency of 4500 Hz, and that our operating frequency should be around 1000 Hz.

Figures 3.11 and 3.12 show the results for the no load case, with lubrication of the contact surfaces of the disc and clamp and without lubrication respectively. The frequency of operation is 1000 Hz. Figures 3.13 and 3.14 summarize the behaviour of the hybrid motor under various torque conditions. For the sake of completeness, table 3.4 gives the specifications of the motor. Figure 3.15 shows the magnitudes of the extensions that we can expect from the Terfenol-D actuator is about 5 microns and that from the PZT actuator is about 2 microns, for an input voltage of 30 V and an input frequency of 1000 Hz.

Figures 3.16 and 3.17 give the characteristic curves of the hybrid actuator for operating frequencies of 800 Hz and 1500 Hz respectively. It is assumed that the motor is unlubricated. Observing figures 3.13, 3.16 and 3.17, we see that as

$A_m \equiv$ Area of the magnetostrictive rod face $= 2.8274 * 10^{-5} sq.m$

$l_m \equiv$ Length of the magnetostrictive rod$= 0.0513m$

$N_m \equiv$ Number of turns of wire on the magnetostrictive rod $= 1300$

$A_e \equiv$ Area of the Electrostrictive stack face $= 1.9634 * 10^{-5} sq.m$

$l_e \equiv$ Length of the electrostrictive stack$= 0.02m$

$N_e \equiv$ Number of layers of the electrostrictive material $= 80$

$R \equiv$ Resistance of the wire on the magnetostrictive rod$= 6.4 ohms$

$R_{ed} \equiv$ Effective resistance of the eddy current loss $= 496.8 ohms$

$M_{clamp} \equiv$ Mass of the clamp $= 0.0085 kg$

$M_{bar} \equiv$ Effective mass of disk obtained from FEM analysis $= 1.044 kg$

$k_{bar} \equiv$ Effective stiffness of disk obtained from FEM analysis $= 7.945 * 10^8 N/m$

$M_{mag} \equiv$ mass of the magnetostrictive rod $= 0.0134 kg$

$M_{piezo} \equiv$ Mass of the electrostrictive stack $= 0.003 kg$

$y_0 \equiv$ Initial separation between the clamp and the disc $= 0.0m$

$A_{clamp} \equiv$ Area of the clamp surface facing the disc $= 4.03 * 10^{-5} sq.m$

$l_{clamp} \equiv$ Length of the clamp $= 2.362 * 10^{-2} m$

$\mu \equiv$ The coefficient of friction between the disc and the clamp (without lubrication) $= 0.5$

$\mu \equiv$ The coefficient of friction between the disc and the clamp (with lubrication) $= 0.2$

$I_{disc} \equiv$ The moment of inertia of the disc and the shaft about their axis $= 9.401e-4 kg/m^2$

Table 3.2: The parameters of the hybrid actuator system.

$\epsilon \equiv$ Permittivity of the piezoelectric material (PZT-4D)$= 3.006 * 10^{-8}$

$\mu^T \equiv$ Permeablity of the magnetostrictive material (TERFENOL-D)$= 1.156 * 10^{-5}$

$s^e \equiv 1/$Young's Modulus of the electrostrictive material$= 2.08 * 10^{-11}$

$d_m \equiv$ Magneto-mechanical coupling constant of the magnetostrictive material$= 1.5 * 10^{-8}$

$d_e \equiv$ Electro-mechanical coupling constant of the piezoelectric material$= 5.93 * 10^{-10}$

$s^h \equiv 1/$Young's Modulus of the magnetostrictive material $= 3.77 * 10^{-11}$

$s^{iron} \equiv 1/$Young's Modulus of steel (the disc material)$= 4.762 * 10^{-12}$

$s^{bronze} \equiv 1/$Young's Modulus of phosphor bronze (the clamp material)$= 9.091 * 10^{-12}$

Table 3.3: The physical constants of the system.

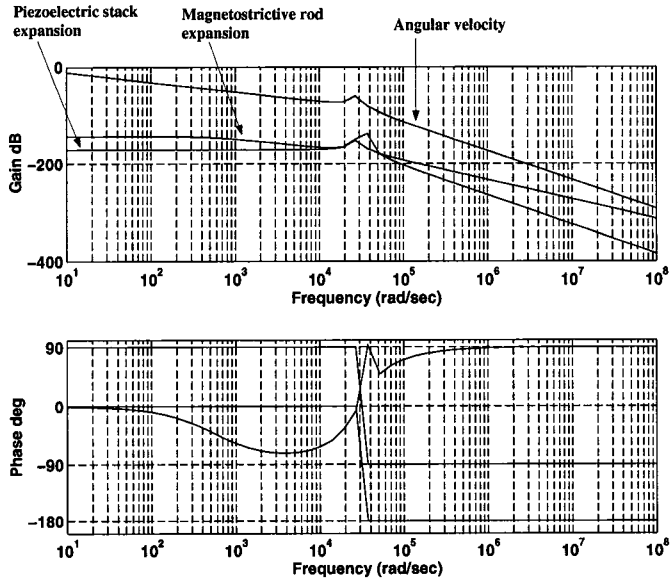

Figure 3.10: Bode plots for the clamped hybrid motor.

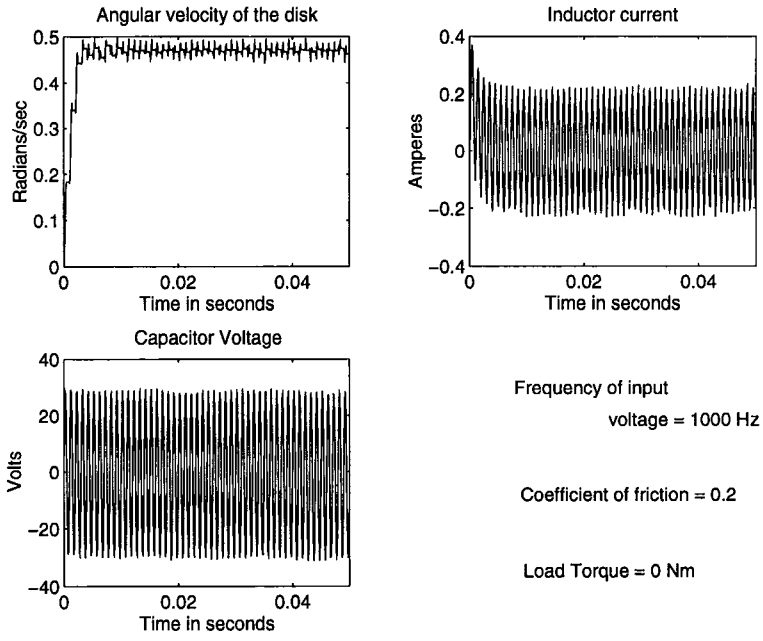

Figure 3.11: Simulation results for the lubricated case.

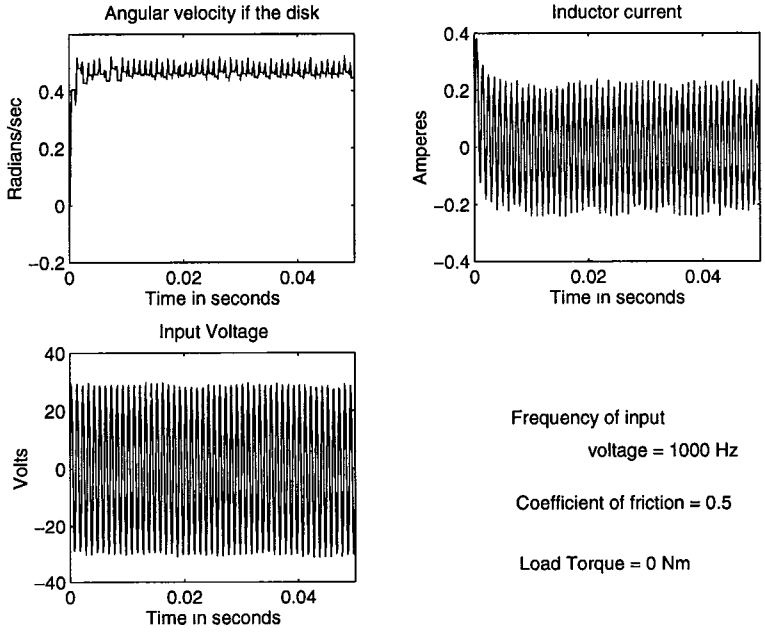

Figure 3.12: Simulation results for the unlubricated case.

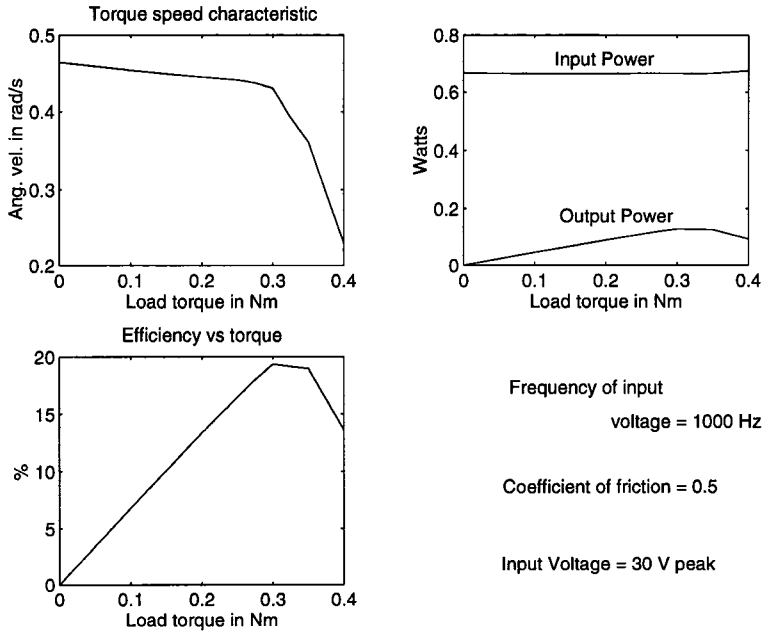

Figure 3.13: Characteristic curves for the hybrid actuator.

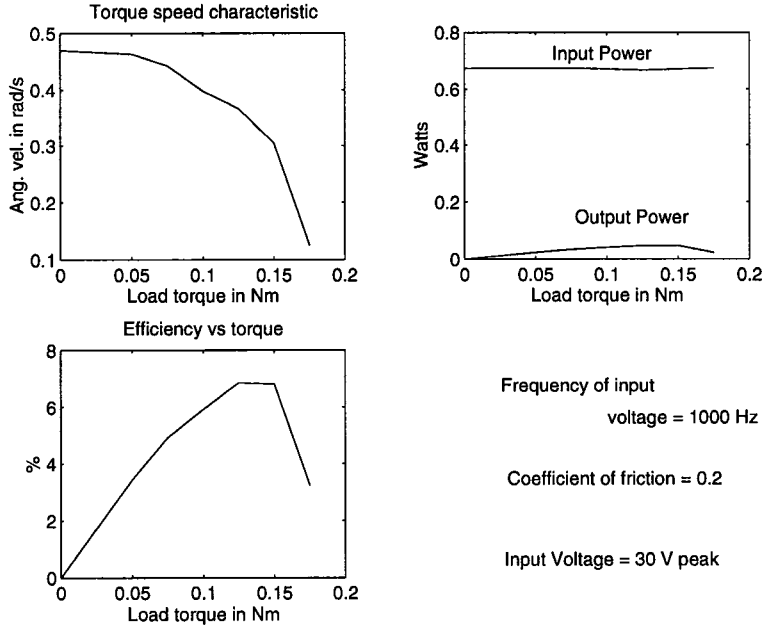

Figure 3.14: Characteristic curves for the hybrid actuator.

	With lubrication	*Without lubrication*
Coeff. of friction	0.2	0.5
Input (peak)	30 V, 0.2 A, 1000 Hz	30 V, 0.2 A, 1000 Hz
No load speed (rpm)	4.4	4.4
Stall torque (Nm)	0.2	0.45
Peak efficiency (%)	6.86	19.34
Conditions for		
peak efficiency	Load = 0.125 Nm	Load = 0.3 Nm
	Speed = 3.50 rpm	2.86 rpm

Table 3.4: Specifications for the proposed hybrid motor.

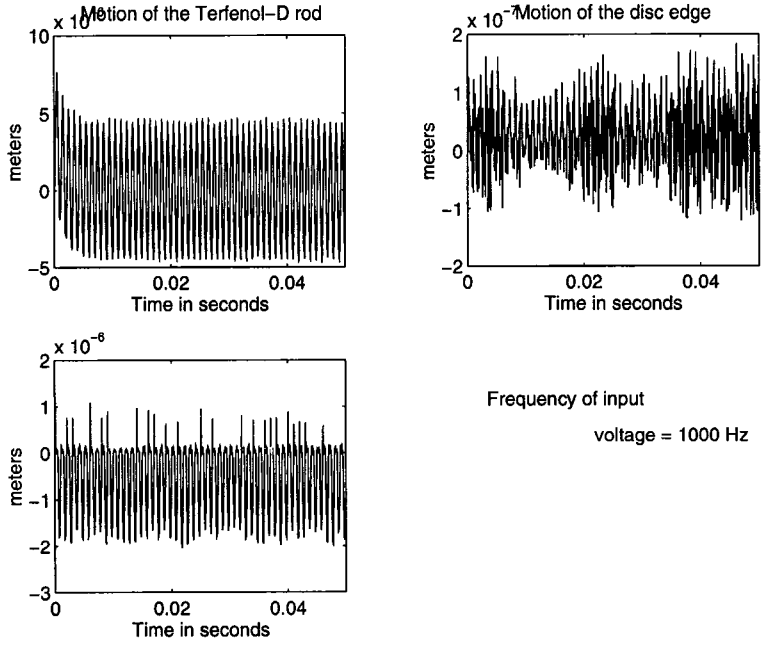

Figure 3.15: Typical displacements of the SMART actuators.

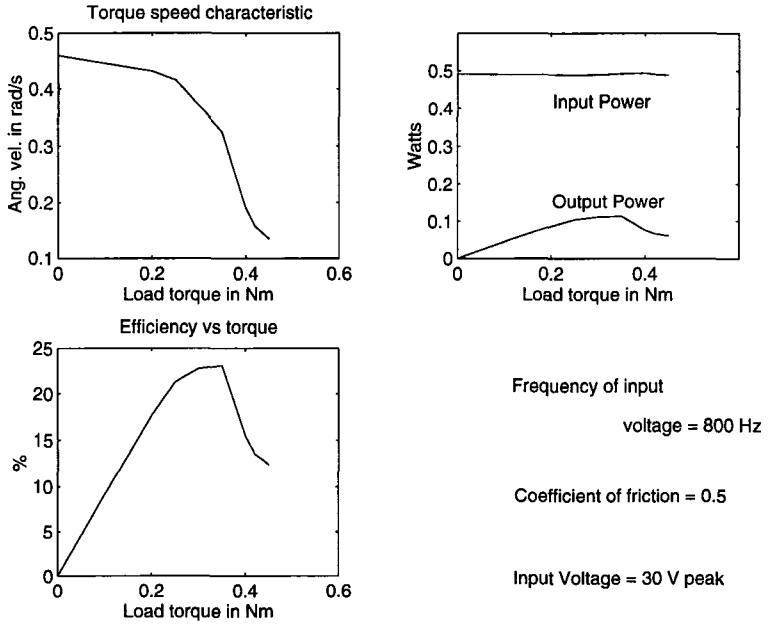

Figure 3.16: Characteristive curves with input frequency = 800 Hz.

the operating frequency increases, the stall torque decreases, while the no load speed increases. The maximum efficiency in all the three cases is about 20%.

Fig. 3.18 shows the typical impact stress on the piezoelectric stack. The typical values of the different variables at impact are $v_{clamp} = 0.03$ m/s, $v_{disc} = -0.01$ m/s, $V = 1$Volt. The yield strength of the PZT-5H ceramic is 345 MPa [19], while the yield strengths of Phosphor bronze and steel is about 131 MPa and 1000 MPa respectively[20]. The impact strength may be much lower. The simulation shows that the typical impact stress is only about 1.6 MPa. Figure 3.19 shows that the stress on the piezoceramic as a function of time is much less than the yield strength.

These results tell us that we are in a reasonably safe operating region as far as the yield strengths are concerned, but for the prototype actuator, we have to keep the force level below the dynamic vertical load capacity of the slide (133

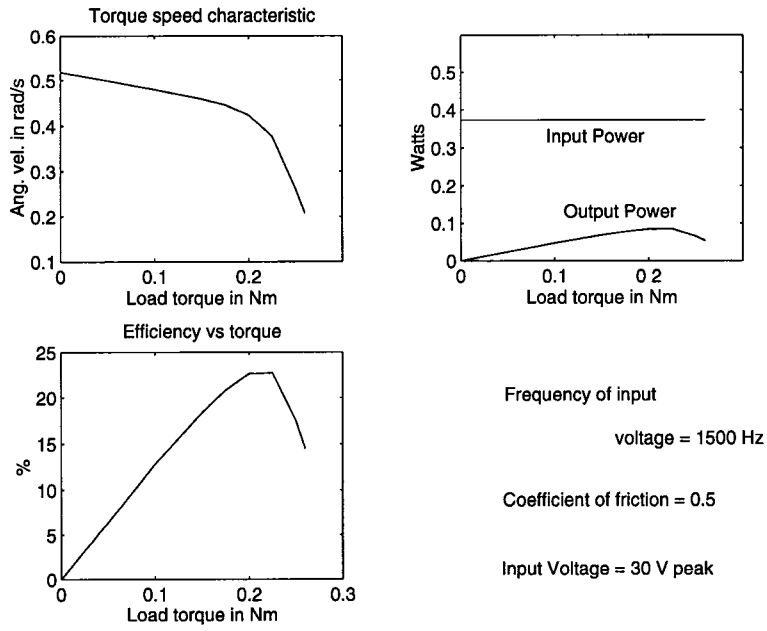

Figure 3.17: Characteristive curves with input frequency = 1500 Hz.

Frequency (Hz)	*Stall Torque (N-m)*	*No load speed (rad/sec)*	*Max. Output Power (W)*	*Maximum Efficiency (%)*
800	0.48	0.460	0.114	22.8
1000	0.45	0.464	0.129	19.3
1500	0.3	0.5184	0.085	22.6

Table 3.5: Comparison of the hybrid motor's performance at various input frequencies.

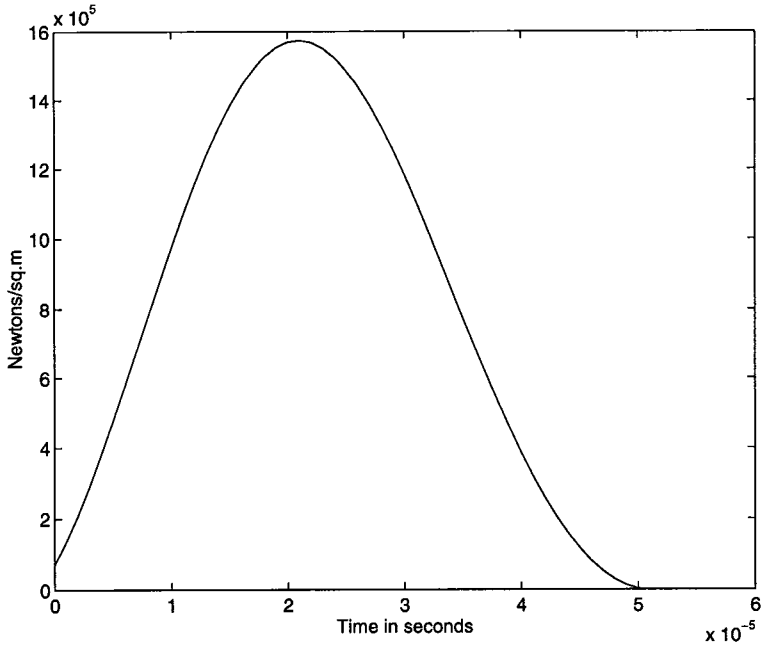

Figure 3.18: Typical impact stress on the piezoelectric stack.

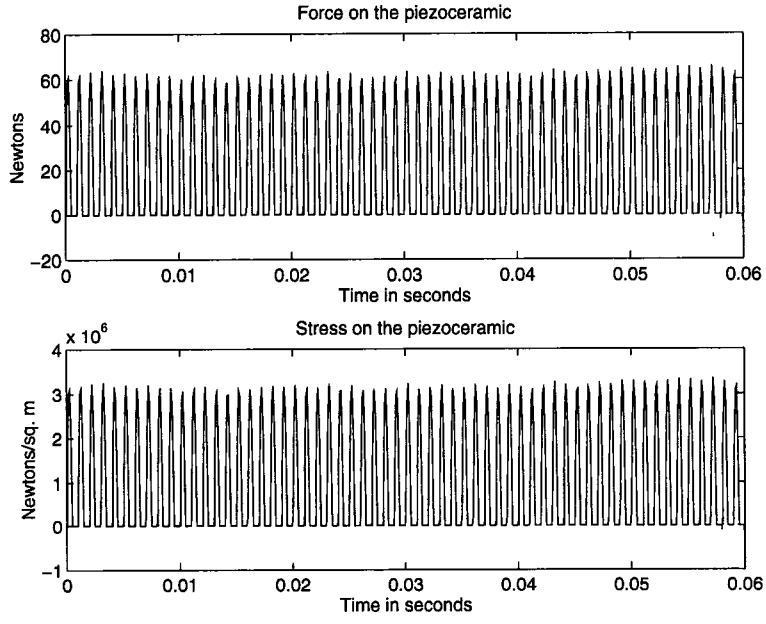

Figure 3.19: Force and stress on the piezoelectric stack vs time.

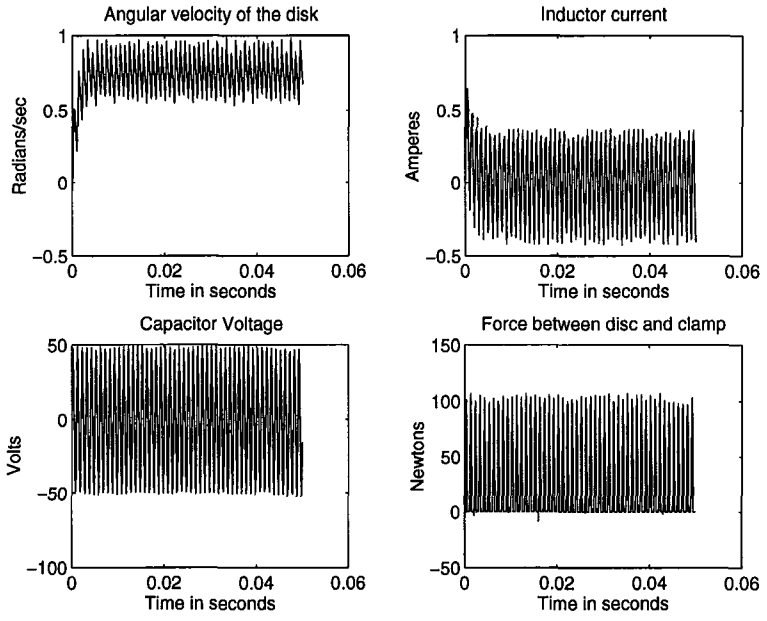

Figure 3.20: Response of the hybrid motor for input voltage = 50 V.

N). Figure 3.20 shows the system response for a input voltage of 50 V with the operating frequency at 1000 Hz. The load torque is 0.45 Nm, which was the stall torque with the input voltage at 30 V. We see that we have an angular speed of 0.72 rad/s, at an efficiency of 26.17%. The force between the clamp and the disc is only 100 N, and the displacements of the Terfenol-D actuator and the PZT actuators are 8 microns and 3 microns respectively.

Chapter 4

An Application Example

The hybrid actuator with a suitable controller can be used in applications with precision positioning requirements. It can also be used in applications with a low-speed and high-torque specification. Its position-hold with power-off capability make it desirable for robotic manipulators. In this chapter, an application of the hybrid motor to helicopter flaperon actuation is presented. First, we consider the problem of achieving bidirectional motion.

4.1 Bidirectional motion

Since we use a parallel resonance circuit for driving the actuator, motion is possible in only one direction. If we switch the magnetostrictive actuators electrically, then we can get the desired mechanical motion in the other direction. In fig. 4.1, switches 1 and 1' are used for motion in say the clockwise direction. While switches 1 and 1' are closed, switches 2 and 2' are open. For anti-clockwise motion, switches 2 and 2' are closed, while switches 1 and 1' are open. Since we have inductors in the circuit, we must have the requirement that the currents are zero when one set of switches are opened and the other set closed. Fig. 4.2 shows a typical timing diagram. Switches have their own operating time (typically 0.5ms

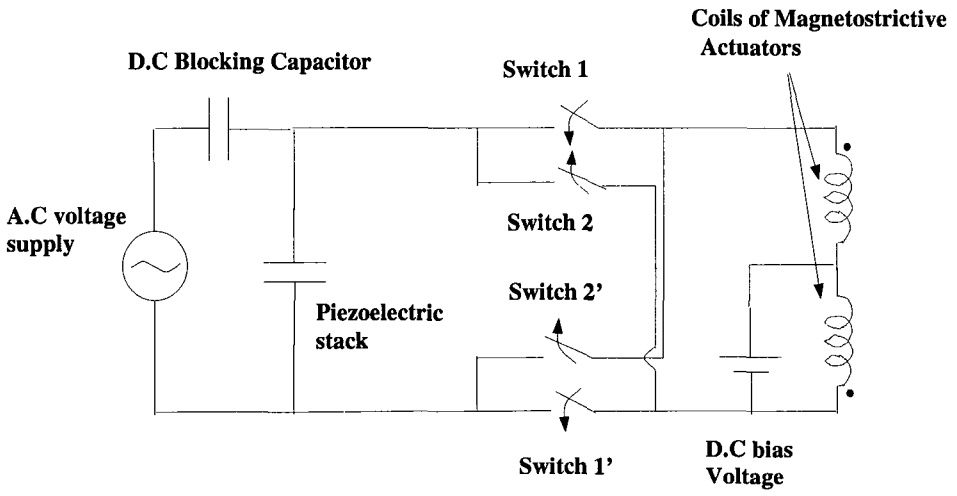

Figure 4.1: Drive circuit for bidirectional motion.

including bounce time), and this has to be taken into account also.

4.2 Helicopter Flaperon Actuation

Helicopters suffer in performance due to harmonic flow variations which result in vibrations in the body[21]. The most common active device to suppress the vibration involves oscillation of blade pitch through excitation of the swashplate with servo-actuators. Such a lift variation can also be accomplished using leading and trailing edge flaps or flaperons. For the flaperon described in [21], the actuator is required to produce an actuation torque of about 0.4 lb-in at 40 Hz. The bimorph and the piezoelectric stack actuators considered were found inadequate for this purpose[21]. Since the hybrid actuator described in the chapter 3 can produce 0.86 lb-in, 3.89 lb-in of torque with and without lubrication respectively, conceivably we can make use of it for this application. Since the limitation on the torque produced by the hybrid motor is due to the limited capacity of the slide used in the design, the previously mentioned stall torques

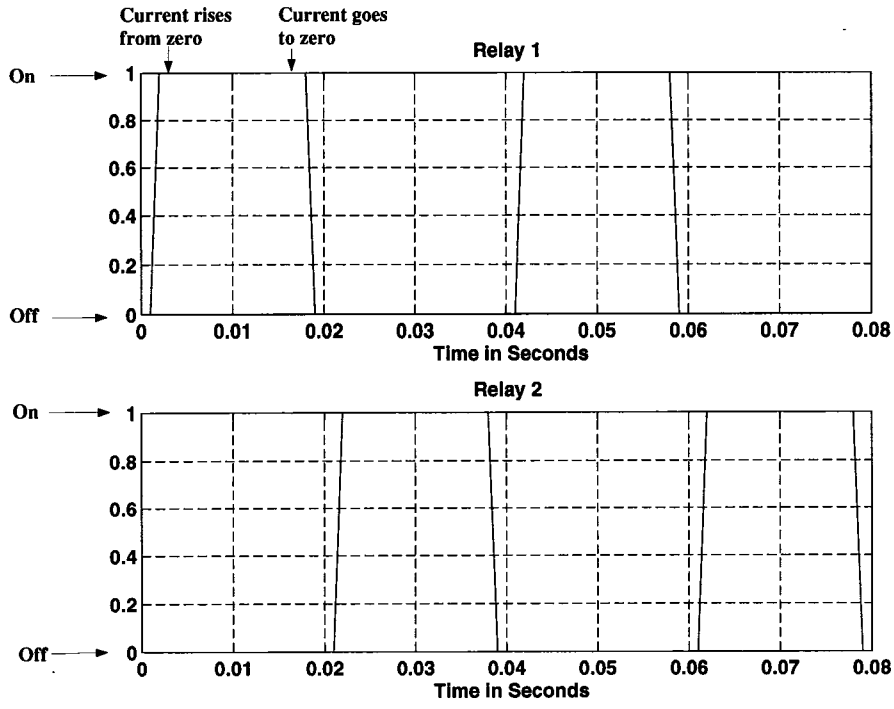

Figure 4.2: Switching waveforms for bidirectional motion .

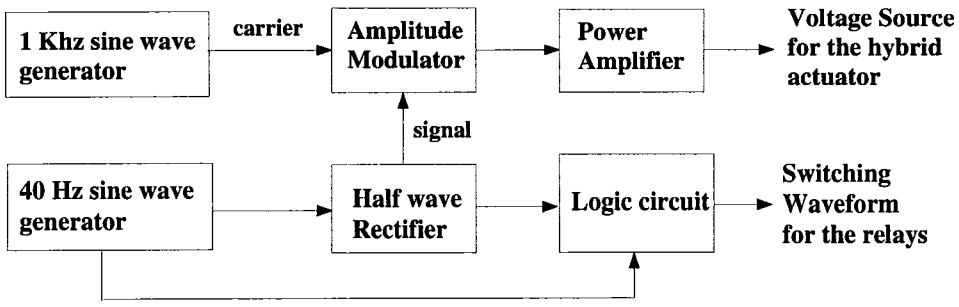

Figure 4.3: Control circuit for flaperon actuation.

can be significantly increased by a better mechanical design.

A block diagram of the control circuit is shown in fig. 4.3. We need a 1 KHz oscillator for operating the hybrid actuator. The amplitude of this waveform has to be modulated as shown in fig. 4.4. From the 40 Hz signal in fig. 4.4, we can generate signals a, $\bar{a}$, b and the amplitude modulating waveform. The signal c is just sign(b). By a logical 'AND' operation, we generate the relay operating signals from c, a, and $\bar{a}$. We see that the amplitude modulating signal dies down to zero before the relays open or close. This signal is then fed to a power amplifier and the output is the voltage source for parallel resonance circuit. Fig. 4.5 shows the circuit diagram for the half-wave rectification of the 40 Hz signal (after a level-sense operation), while fig. 4.6 is a circuit diagram for the amplitude modulation[22].

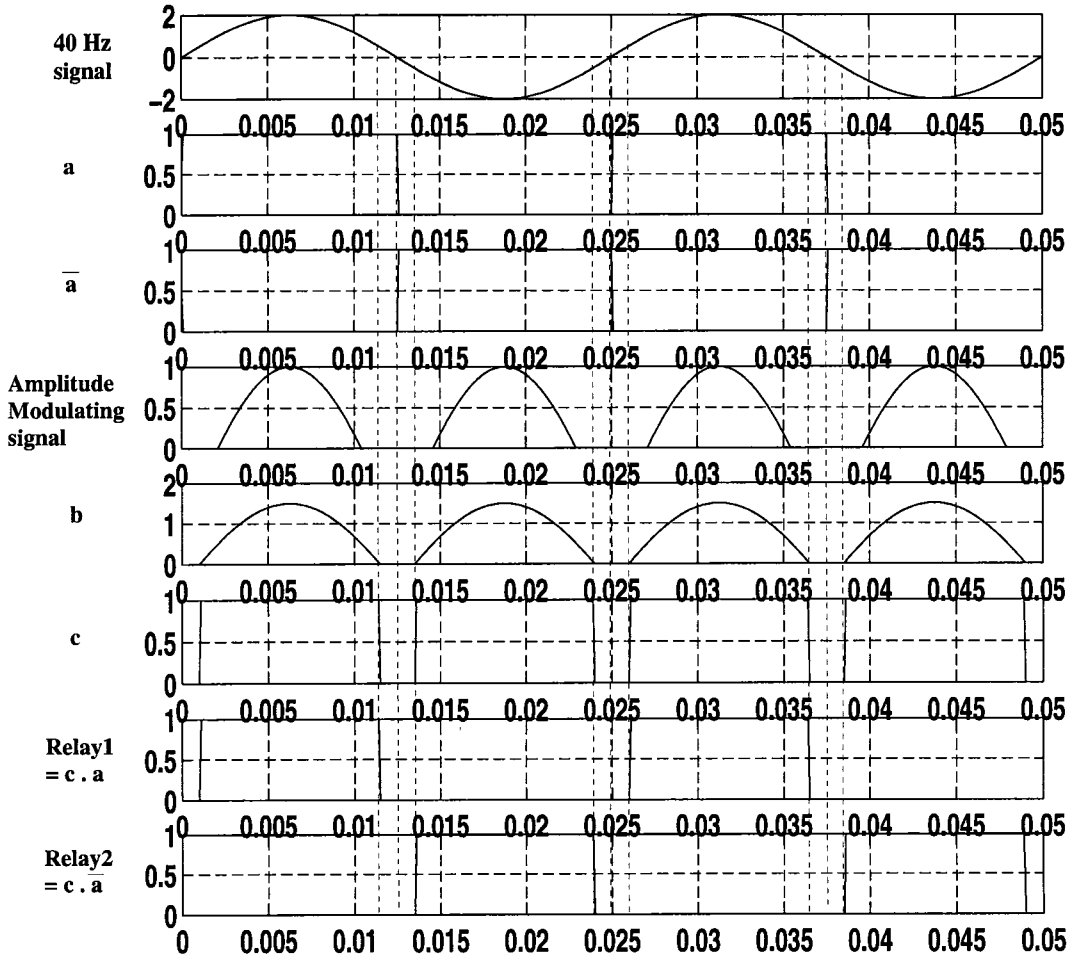

Figure 4.4: Timing diagram for flaperon actuation.

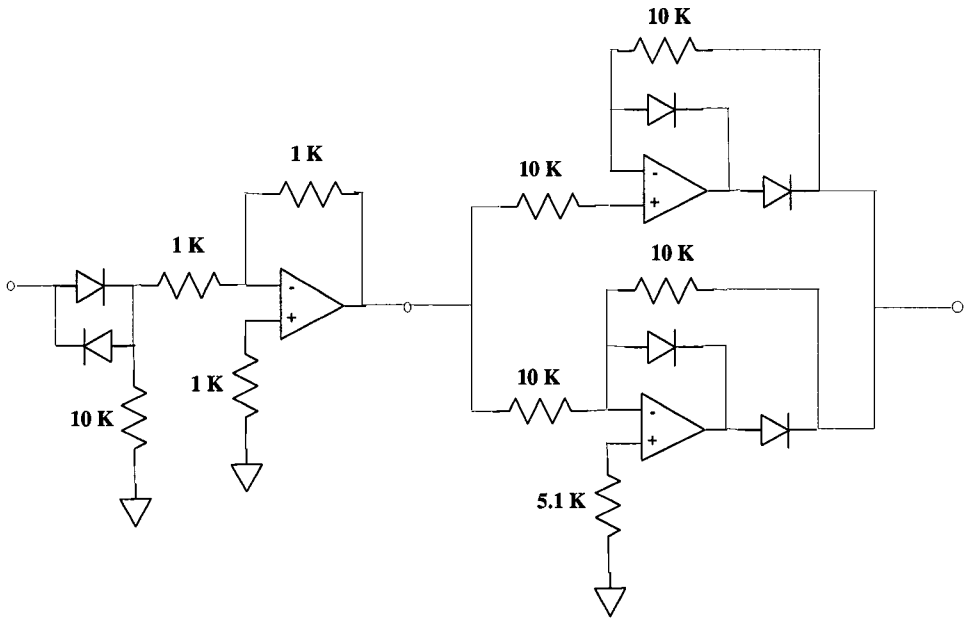

Figure 4.5: Circuit for level sensing and half wave rectification.

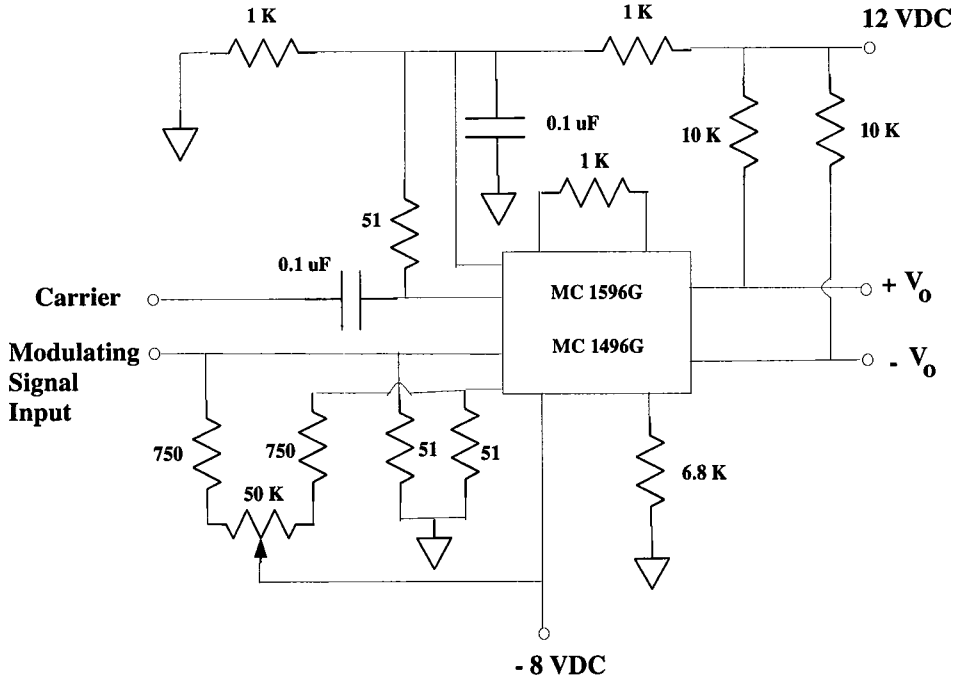

Figure 4.6: Circuit for amplitude modulation.

Chapter 5

The Prototype Hybrid Actuator

The aim of the prototype is to show proof of concept. Hence small size of the actuator was not considered a priority and commercially available components were used as much as possible to keep the cost low. Though the basic scheme of the hybrid actuator is simple, the constructional details of the prototype is quite complex. Since the elongation of the piezoelectric stack and the magnetostrictive actuator is in the order of microns, initial adjustments are crucial to the actuator's performance. To be able to make the required adjustments and keep the cost of the actuator low, a compromise has to be made regarding simplicity of design.

The actuator itself can be thought of being comprised of two halfs—a top half and a bottom half (figs. 5.1 and 5.2). The top half consists of the piezoelectric stack, the two magnetostrictive actuators, the clamping piece, and the top slide for aligning the axis of the piezoelectric stack with the center-line of the disc. The bottom half consists of the disc. The two halfs are joined by a vertical slide which is used to position the clamp against the disc. The positioning device in both the slides is a differential screw which has a resolution of 1 micron. This makes accurate positioning possible.

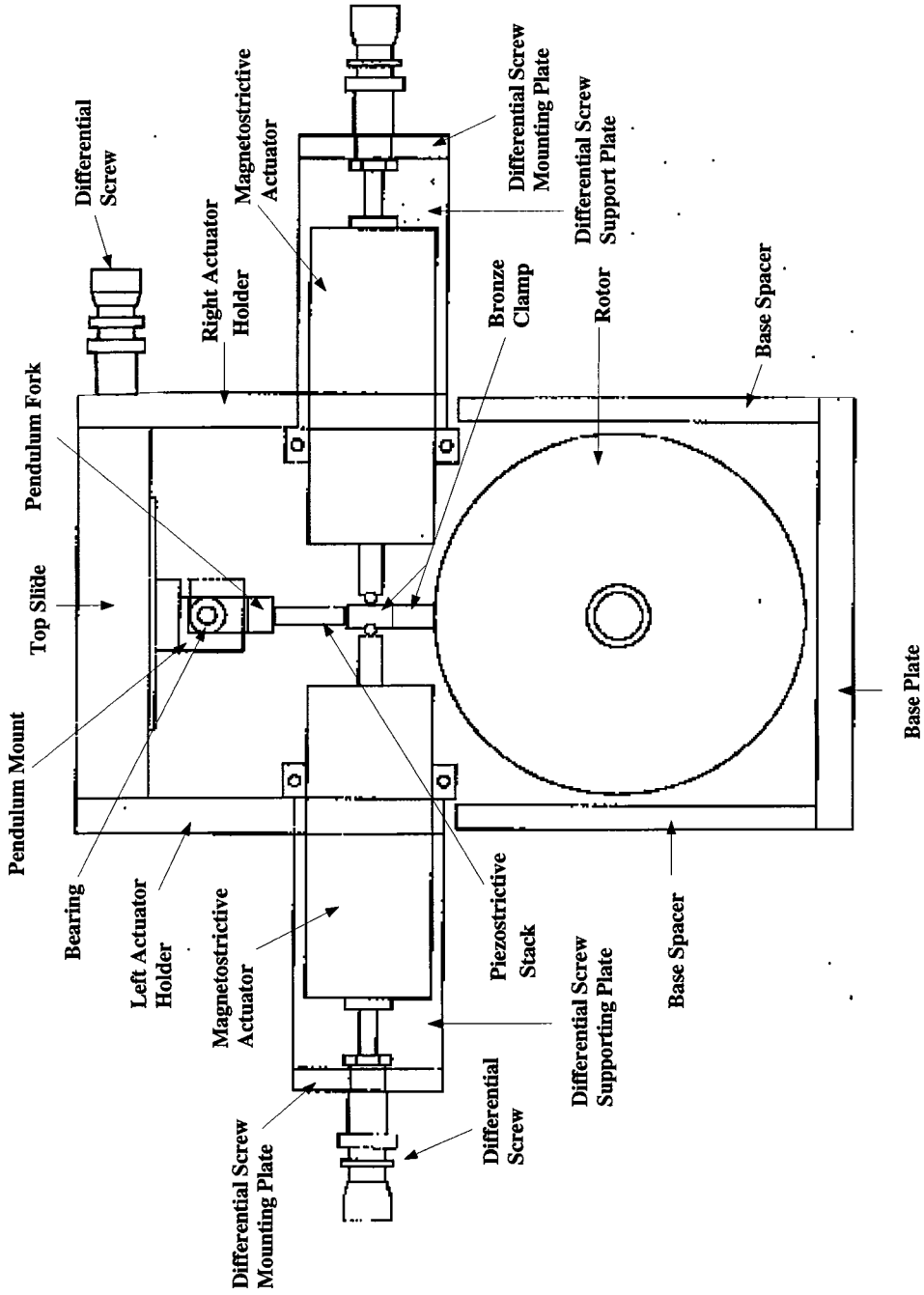

Figure 5.1: The front view of the hybrid actuator.

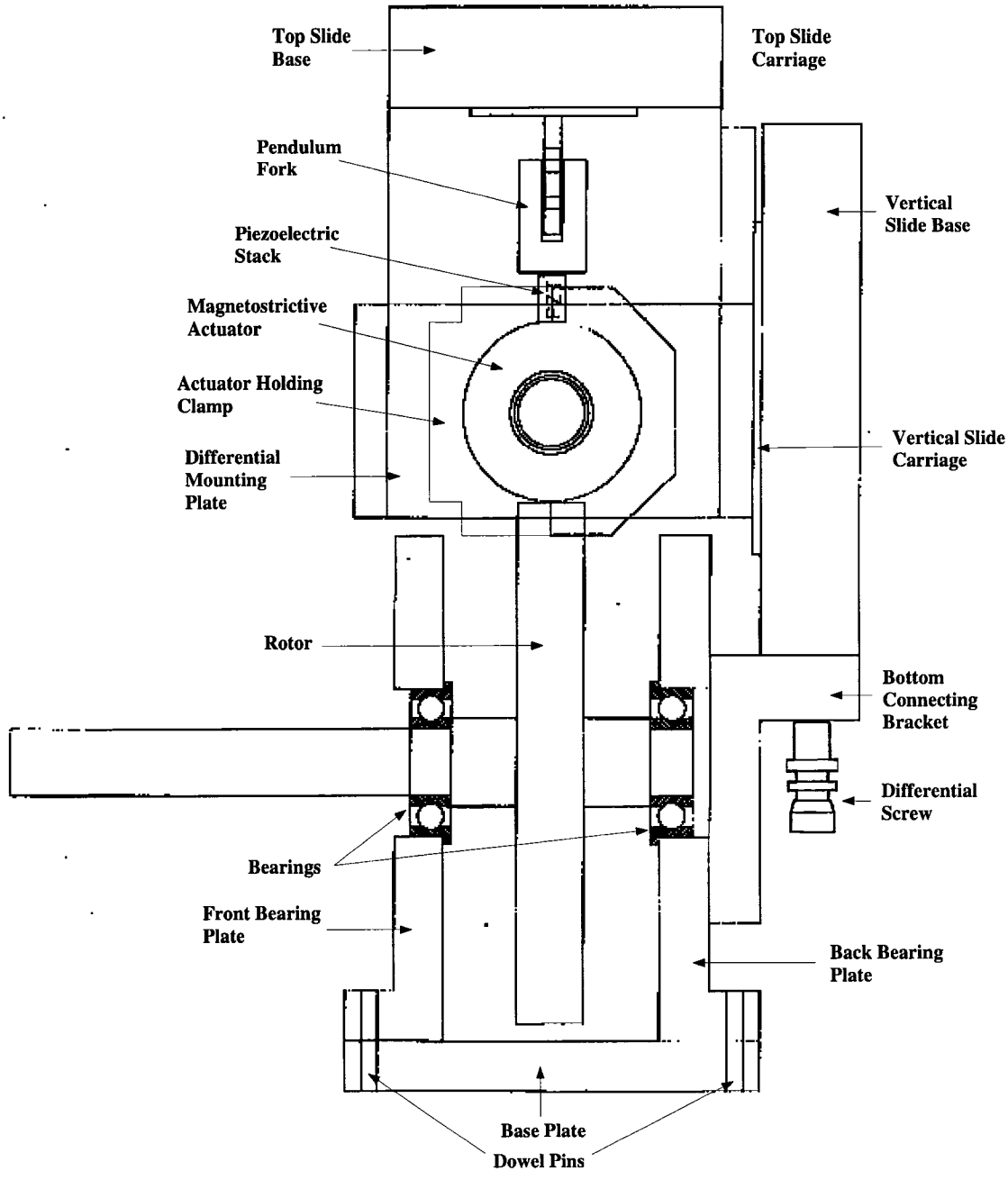

Figure 5.2: The side view of the hybrid actuator.

5.1 The Standard Components

Before we go on to a complete constructional description of the hybrid actuator, we take a look at the commercially available components.

5.1.1 The Piezoelectric Stack

The stack is made of the standard PZT-5H material of Morgan Matroc Inc. It is 5mm in diameter and 20mm in height [19]. There is a ceramic insulation layer at each end of the actuator which is 0.635mm thick. It has a dielectric coating and two soldered 28 gauge copper wire leads. In the hybrid actuator it is glued to the clamping bronze piece on one end and to the slide on the top via a mechanism that allows the stack to swivel. This will be described in a later section.

5.1.2 The Magnetostrictive Actuators

The magnetostrictive rod needs a D.C bias and a prestress, to get it to work in the linear range. ETREMA Products Inc. markets a 50/6 MP magnetostrictive actuator which incorporates a permanent magnet and preloaded springs. Fig. 5.3 shows the cross-section of this actuator. The unit length is 10 cm and the unit diameter is 3.4 cm. The housing is made of aluminum while the push-rod which is the moving unit is made of stainless steel. The length of the Terfenol-D rod is 5.13 cm and its diameter is 0.6 cm. The prestress is adjustable from 0 to 3 Kpsi while the permanent magnet bias is approx. 425 Oe. Its rated load is 490 N. Two such units are required by the hybrid actuator, and it is neccesary for them to be exactly matched for successful operation. The displacement of the push rod vs the input current for the two actuators are shown in figs. 5.4

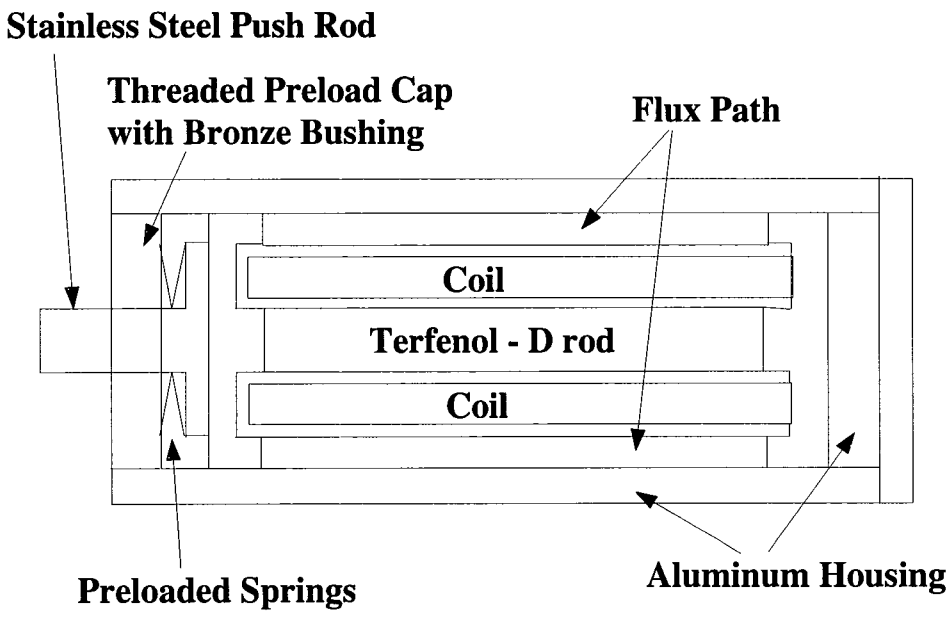

The ETREMA 50/6 MP actuator

Figure 5.3: Cross-sectional details of the magnetostrictive actuator.

and 5.5 respectively. The matching can be achieved by using LVDT sensors, as explained later.

5.1.3 The Slide

The slide is required for aligning the axis of the piezoelectric stack with the centerline of the rotor. Velmex Inc. manufactures slides with a dove-tail base, which is particularly useful for our application. The base is made of hard aluminum alloy. The sliding carriage has low friction polymer bearing pads bonded to it for smooth travel and no side play (fig. 5.6). The base has been modified to enable two screws to fix it to the actuator assembly. The model A2504 slide has

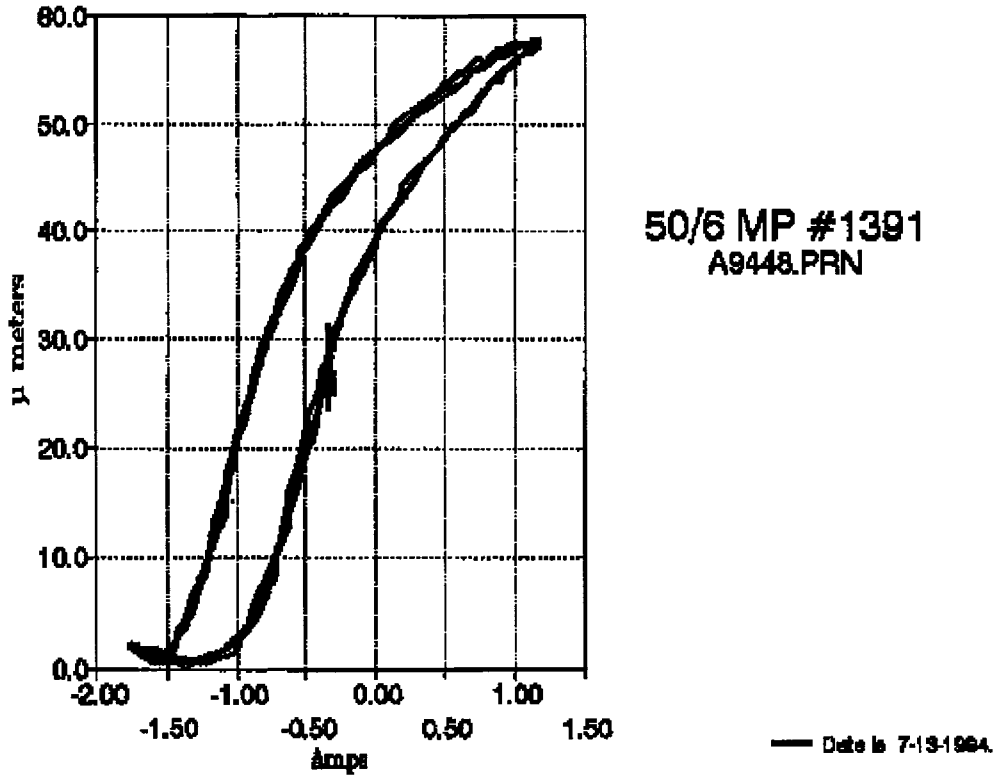

Figure 5.4: The displacement vs input current curve for actuator 1.

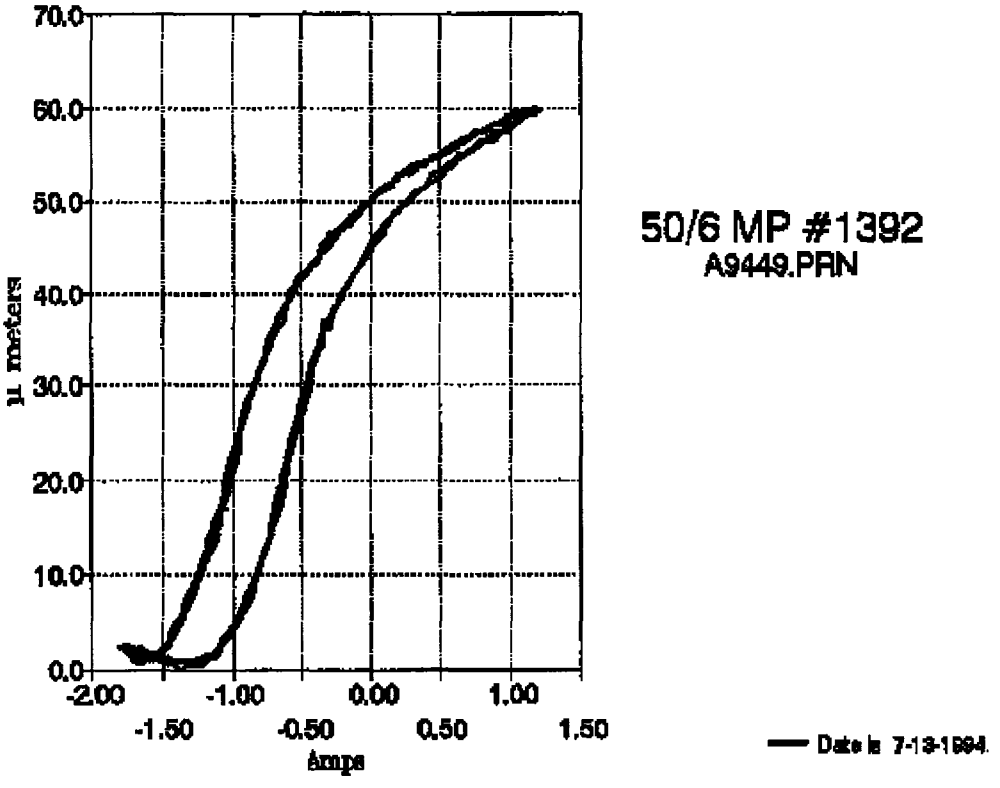

Figure 5.5: The displacement vs input current curve for actuator 2.

a dynamic central horizontal load capacity of 30 lbs., and its dynamic central vertical load capacity is 15 lbs. The cantilevered load capacity is 40 lb-in.

Slides with bearings are very difficult to lock in a position, once the positioning has been achieved. On the other hand, dovetail sliding carriages can be jammed against the side-wall to achieve a good position lock. However this is not the mechanism used in the hybrid actuator for position locking because polymer bearing pads may be worn out by the locking action. The slides have been modified to have two screws locking the carriage in place. The end plate of the slide has been made thicker, so that the slide is now more sturdy. The top slide carriage has four through holes, through which screws fasten the 'Pendulum Mount' to a plate with threaded and tapped holes. This plate fits between the slide carriage and the slide base(fig. 5.7, fig. 5.9). The vertical slide carriage has four through holes, through which screws fasten the 'Back Plate' to another plate with fits between the carriage and the base of the slide(fig. 5.8, fig. 5.10). The holes on the top slide are closer together to take care of the reaction force of the clamp pushing against the disc, while the holes on the vertical slide are more spread out to bear the weight of the top half. The slides have no lead screw, and a differential screw is used for positioning. The differential screw pushes against the plates between the carriage and the slide, because we want the steel end of the differential screw to move against the steel plate. The slide carriage on the other hand is made of aluminum.

5.1.4 The Differential Screw

For the prototype hybrid actuator to function successfully, the centerline adjustment and the clamp position adjustment mentioned before have to be done pre-

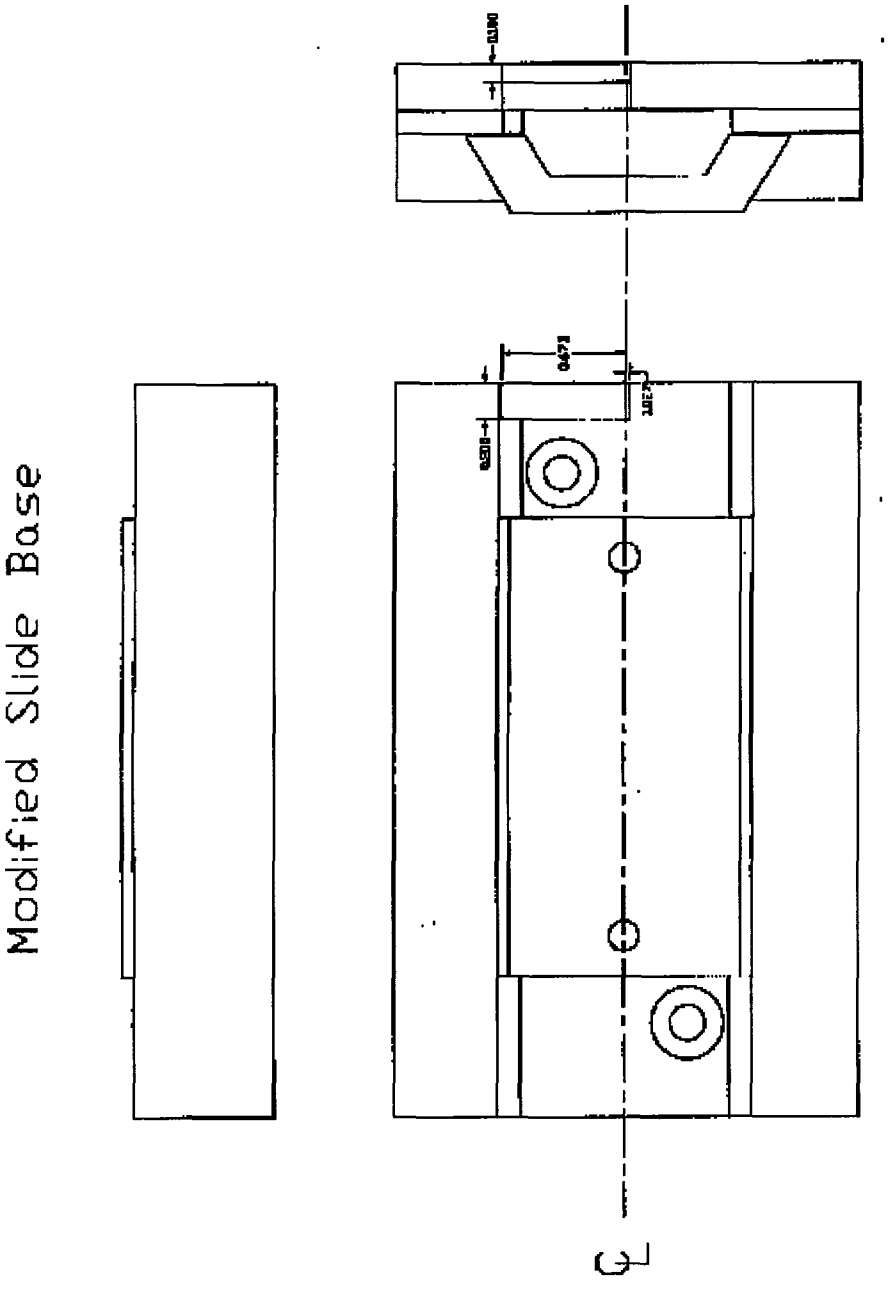

Figure 5.6: The modified slide base.

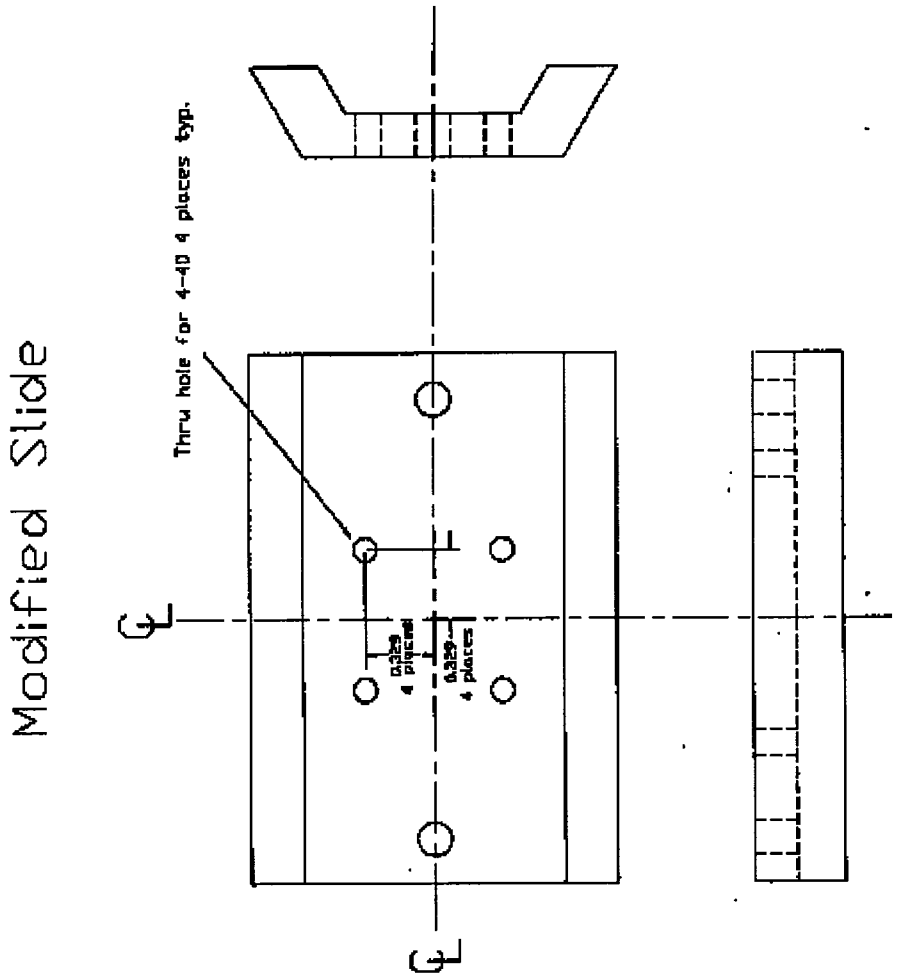

Figure 5.7: The modified top slide carriage.

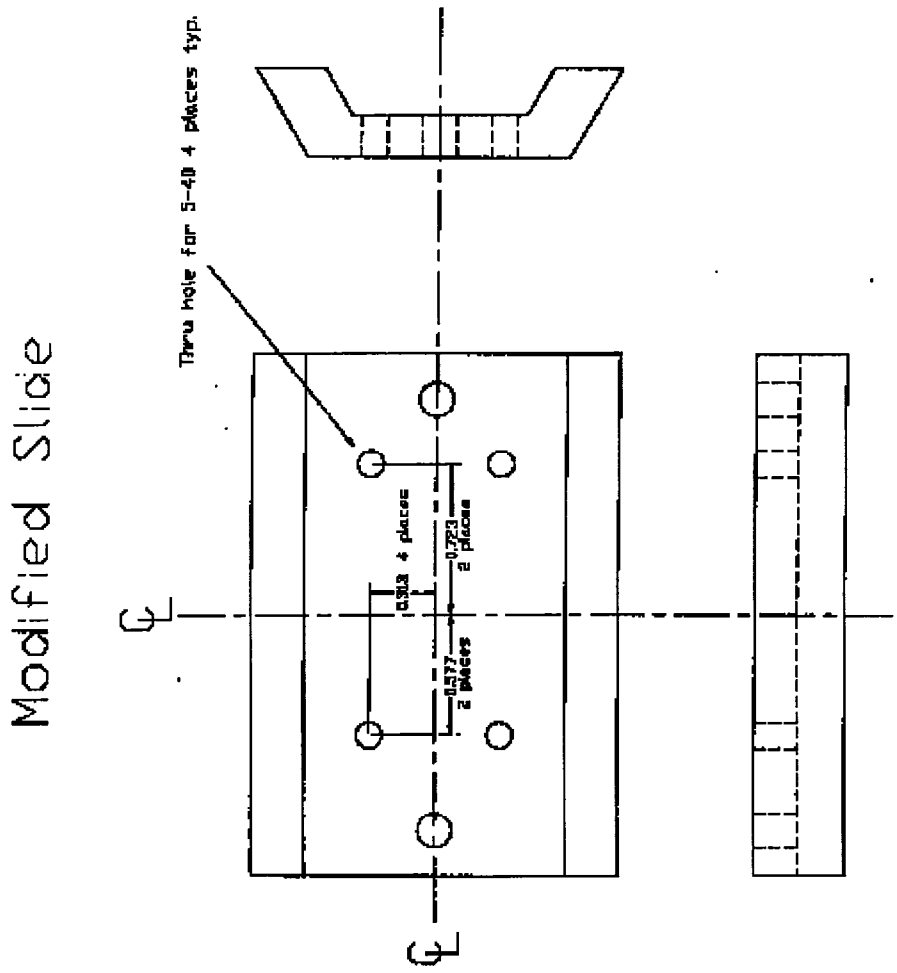

Figure 5.8: The modified vertical slide carriage.

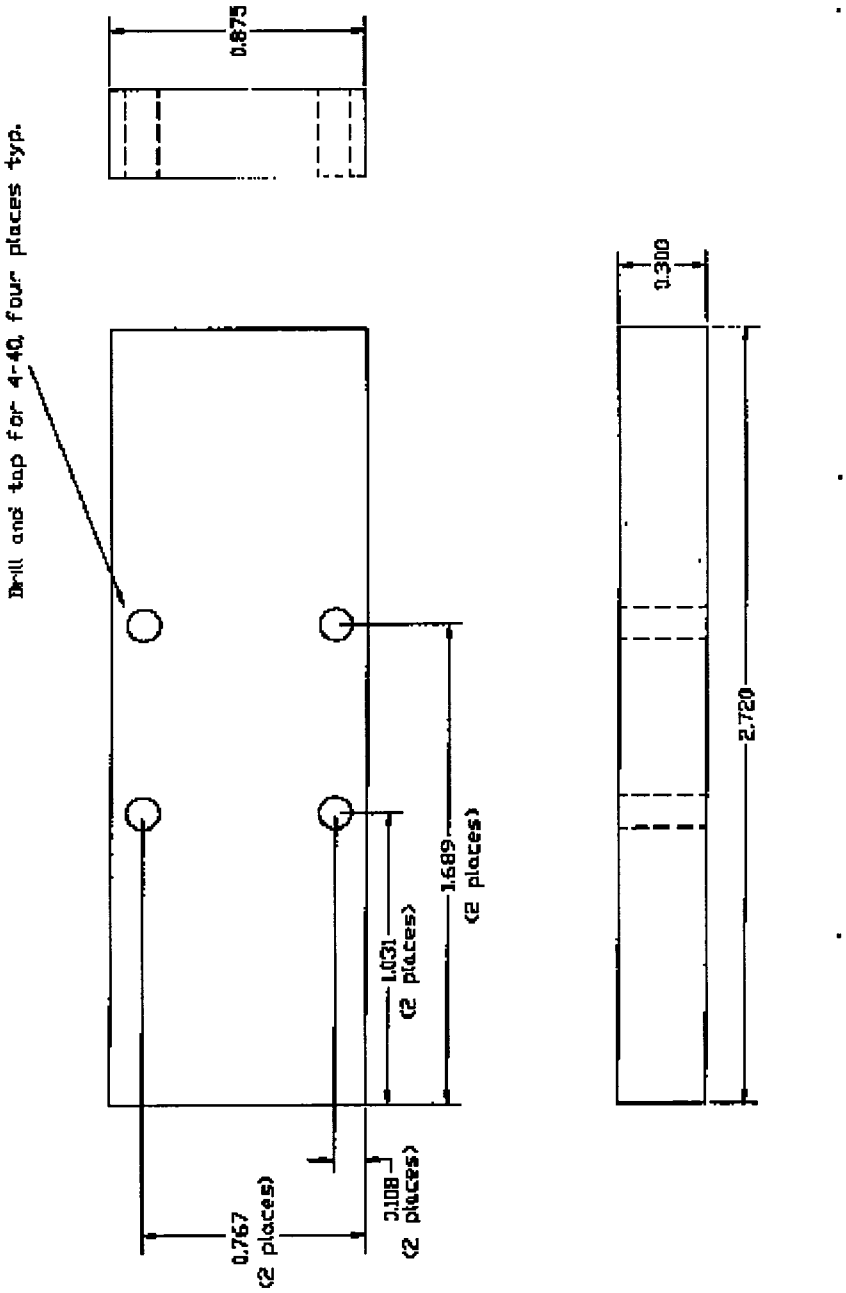

Figure 5.9: The mounting plate for the pendulum mount.

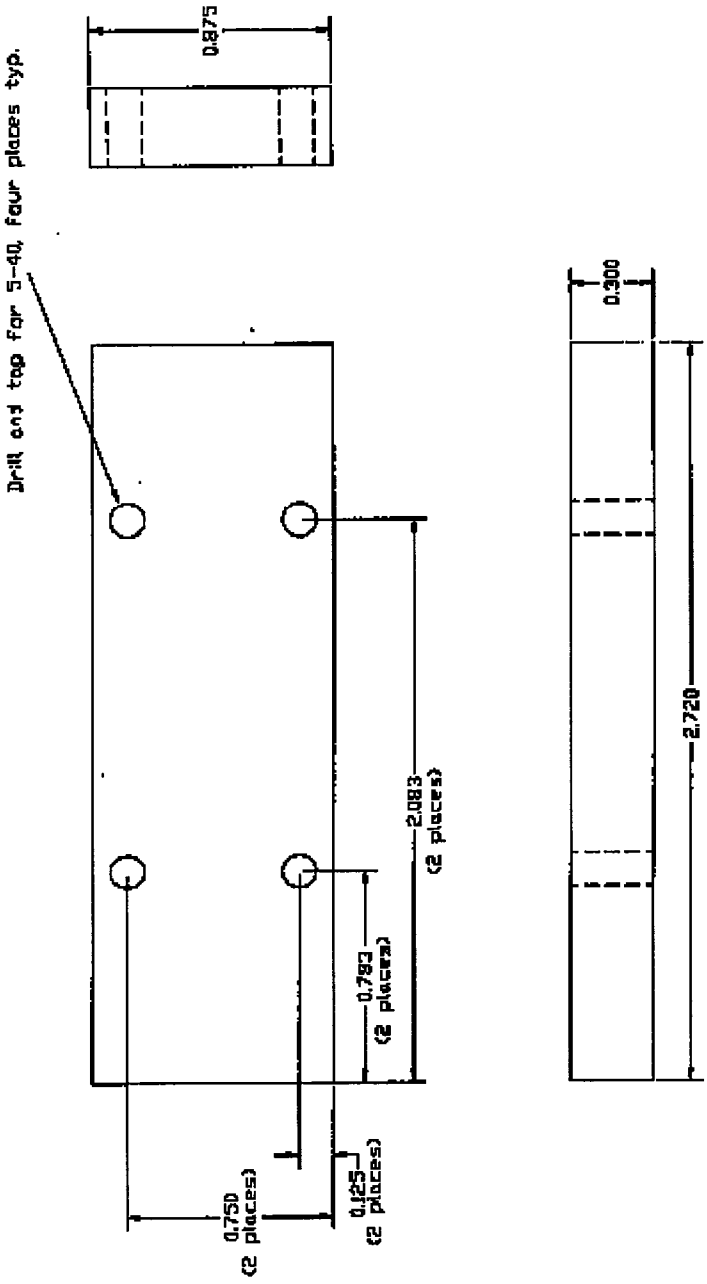

Figure 5.10: The mounting plate for the back plate.

cisely (with accuracy of about 1 micron). In addition, the two magnetostrictive actuators have to be aligned without any slack. The Model 9560 Differential Screw made by Daedal Inc. offers a 1 micron resolution over a 2 mm range (fig. 5.11). The coarse adjustment has a 4 micron resolution over a 8 mm range. The coarse adjustment has a lock, while the fine adjustment has none.

5.1.5 The Bearings

There are three ABEC-7 bearings in the assembly–two of which are required for the rotor and the third is for the swiveling motion of the piezoelectric stack. ABEC-7 bearings are required because we cannot let the axis of the rotor move radially, by more than 3 microns. Similarly the piezolectric stack should not move axially by more than 3 microns. They are marketed by W.M. Berg Inc. and their stock numbers are B2-22-S and B1-25 respectively. We also need SV-4 bearing preload springs for the lower half bearings, while the upper half bearing requires a SS1-21 shaft spacer, all marketed by the same company.

5.2 The Top Half

The front portion of the top half is open, so that visual inspection of the actuator action can be done. The main functional components of the top half of the assembly are the magnetostrictive actuators, the piezoelectric stack, the top slide and the bronze clamp. These (except the bronze clamp) have been described in the section before. What remains is how they have been put together. The structural components have been made rectangular as much as possible, so as to keep machining costs as low as possible. These components for the top half are

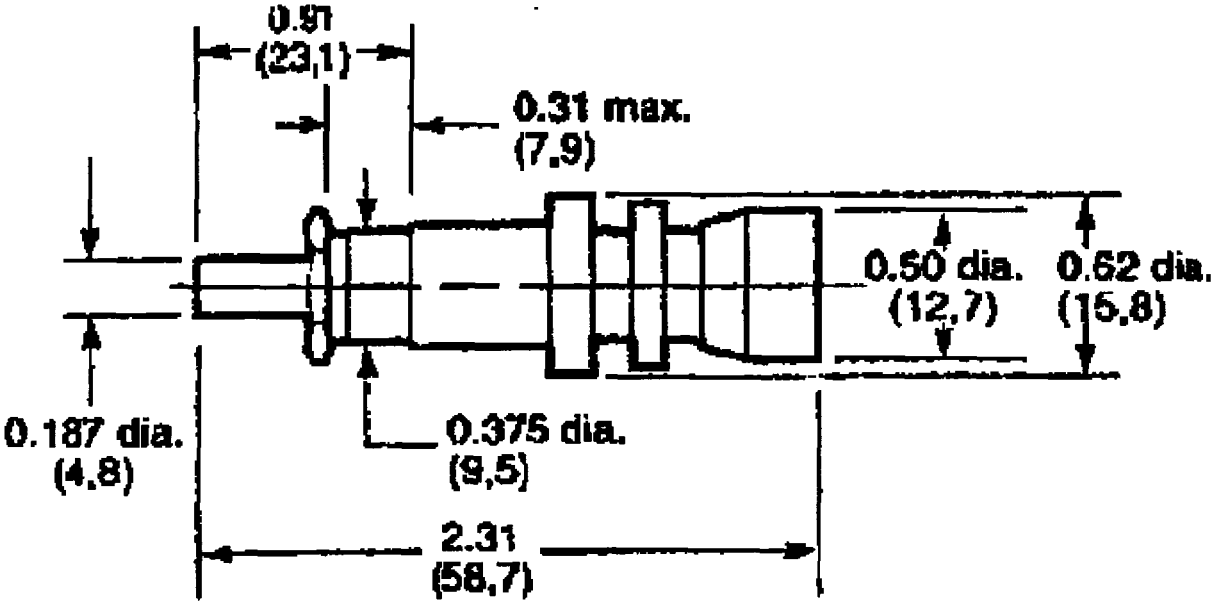

Figure 5.11: The differential screw.

(figs. 5.1 and 5.2) the back plate, the right and left actuator-holding plates, the actuator clamps (2), the differential screw mounting plates (2), the differential screw support plates (2), the pendulum bearing mount and the pendulum fork. Here the pendulum refers to the piezoelectric stack, the bronze clamp and the mechanism that allows it to swivel.

5.2.1 The Back Plate

This is the largest structural component of the top half. As the name suggests, it is to the back of the assembly, with the front being open. It is connected to the vertical slide by four screws at the center of the plate (fig. 5.12). As the figure shows, it has through holes for connecting it to the right and left actuator-holding plates, and tapped holes for connecting it to the differential mounting plates.

5.2.2 The Actuator-holding plates

These form the sides of the top half (fig. 5.1). They have a large hole each for the magnetostrictive actuators to pass through (figs. 5.13 and 5.14). Since the magnetostrictive actuators are heavy, they need to be supported at their axial center. This is done by the actuator-holding plates. The plates have tapped holes for connecting it to the back plate and the differential screw support plates. The top part of these plates forms the end plate of the top slide. Two holes are needed to fix them to the top slide, while another is needed for the external locking screws of the slide to pass through. An extra hole is needed for the right actuator-holding plate to allow the differential screw of the slide to pass through.

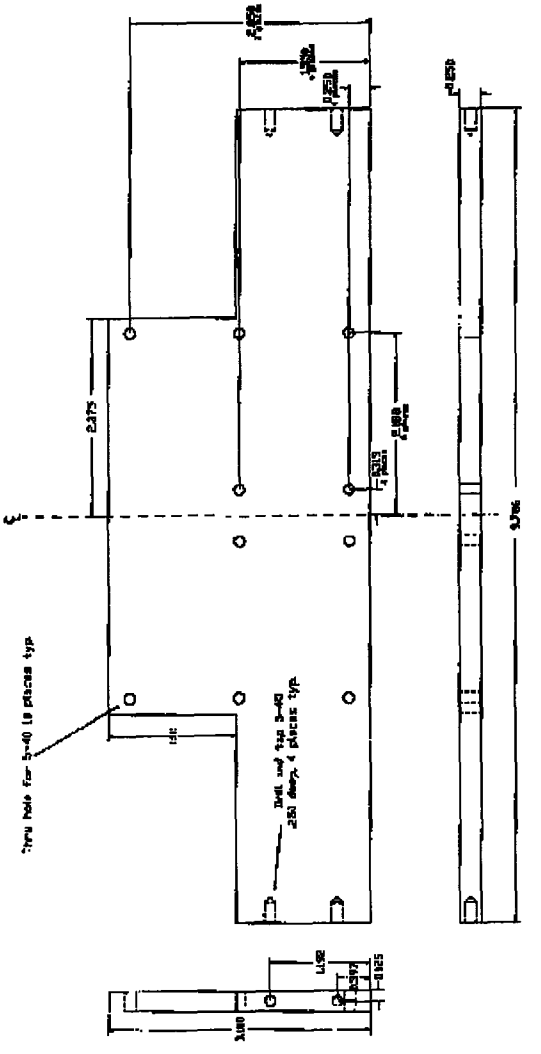

Figure 5.12: The back plate .

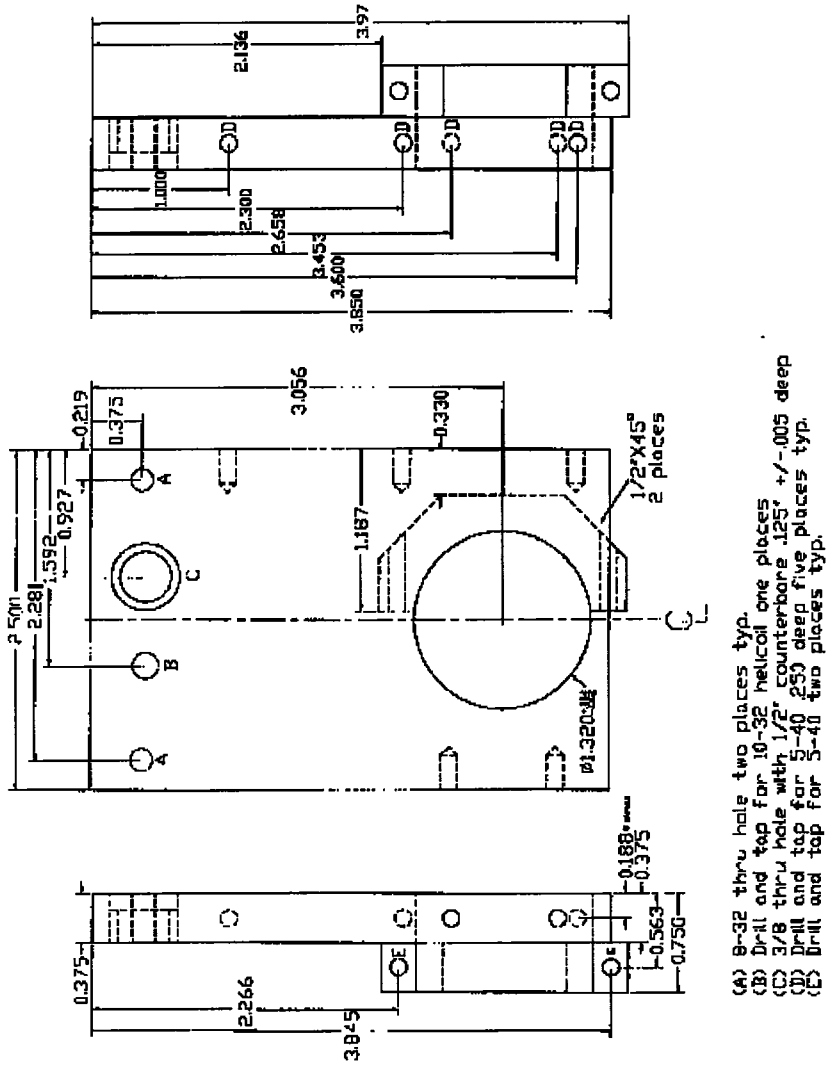

Figure 5.13: The right actuator-holding plate.

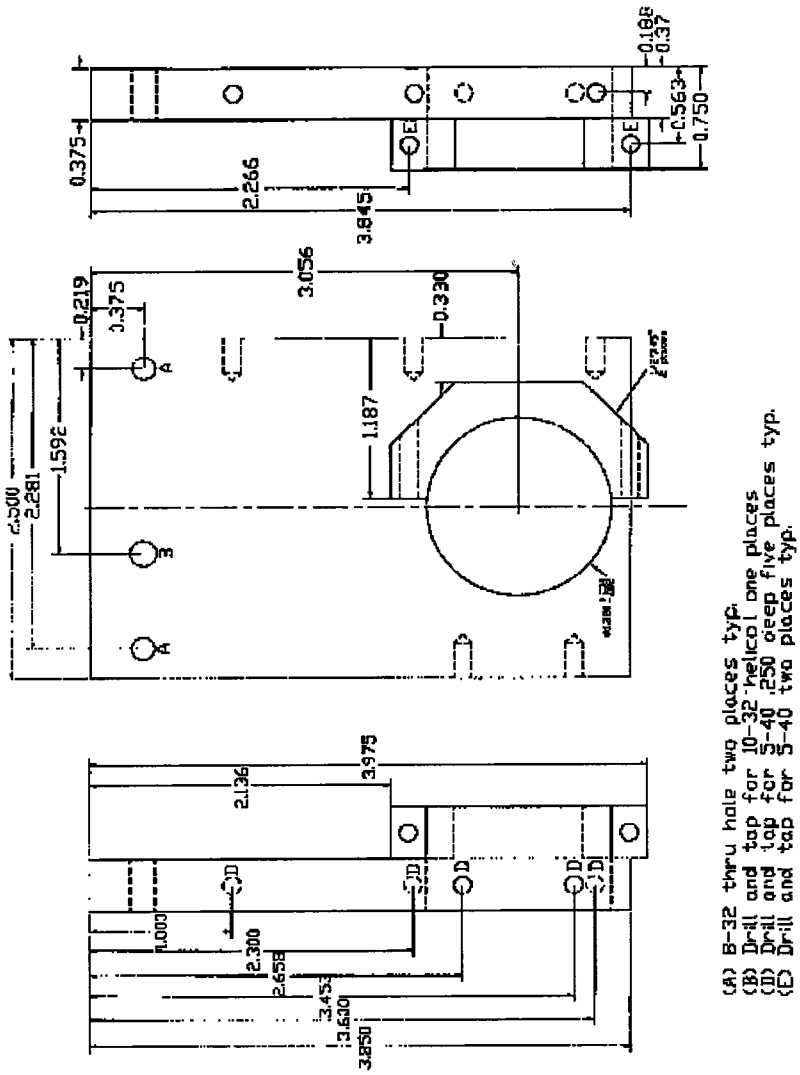

Figure 5.14: The left actuator-holding plate.

5.2.3 The Actuator Clamps

These are needed to snugly fix the magnetostrictive actuators to the actuator-holding plates (fig. 5.15).

5.2.4 The Differential Screw Mounting Plates

These are needed to mount the differential screw to the assembly (fig. 5.1). These have a hole in the center for the differential screw (fig. 5.16).

5.2.5 The Differential Screw Supporting Plates

These form the front of the top half (fig. 5.1). As the name suggests, they provide additional support to the differential screw, by connecting the differential screw mounting plates to the assembly (fig. 5.17).

5.2.6 The Pendulum Bearing Mount And The Pendulum Fork

As mentioned before, the term *pendulum* refers to the piezoelectric stack, the bronze clamp and the mechanism that allows it to swivel. The part of the mechanism connected to the top slide is the pendulum bearing mount. As the name suggets, the top half bearing is press fit into this piece (fig. 5.18). A small shaft passes through the bearing and it is press fit into the pendulum fork (fig. 5.19). The piezoelectric stack is glued onto the base of the fork. This sturdy mechanism allows the stack to swivel, so that the extension of the magnetostrictive actuator does not impose high shear stresses on the stack.

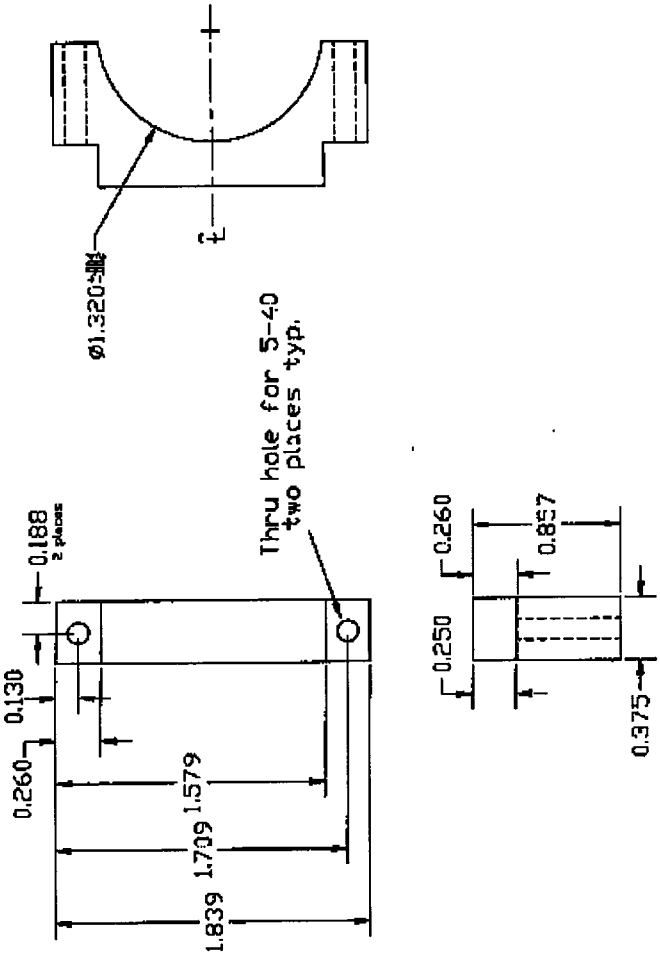

Figure 5.15: The magnetostrictive actuator-clamps.

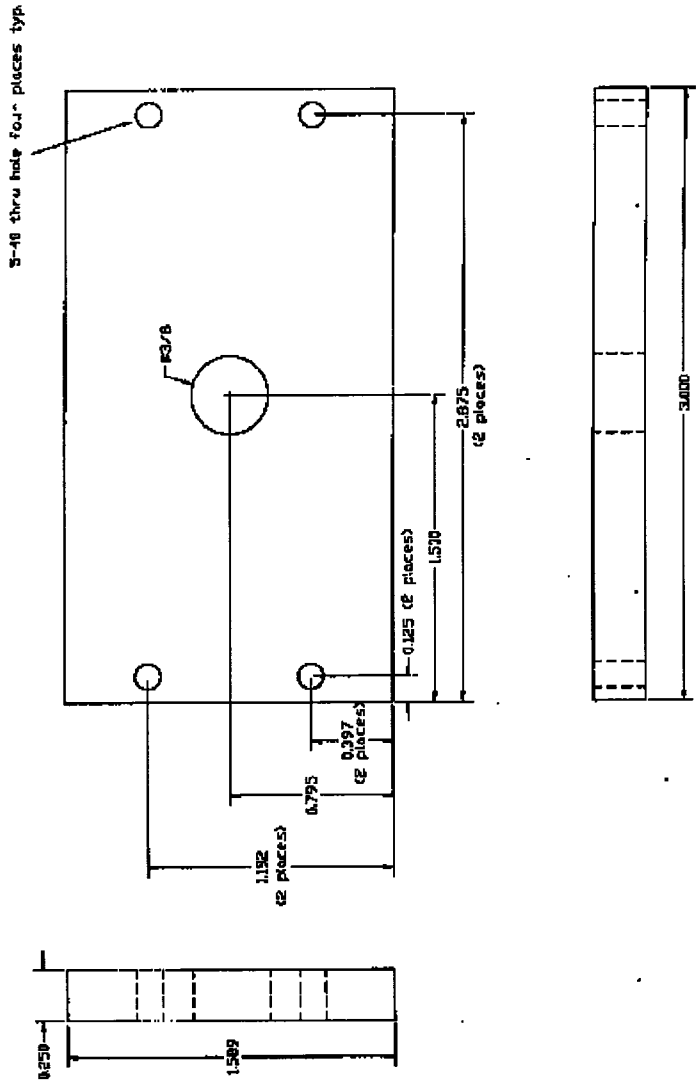

Figure 5.16: The differential screw mounting plates.

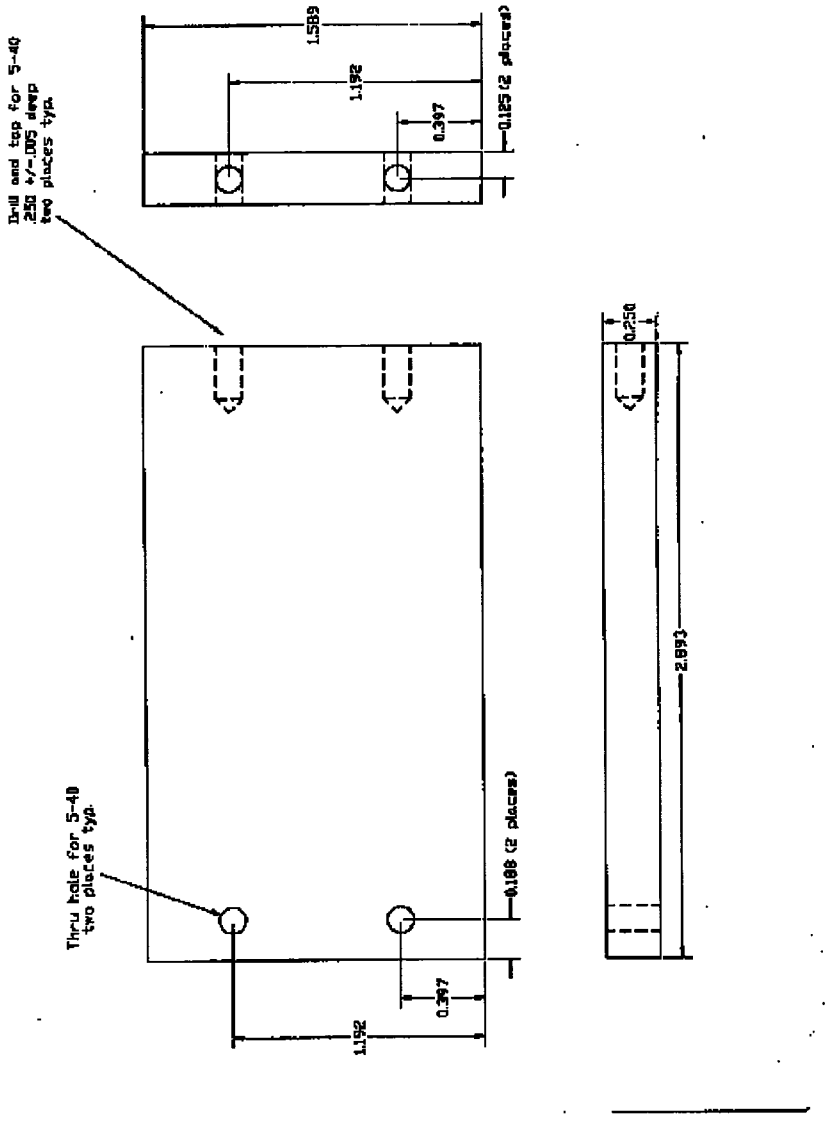

Figure 5.17: The differential screw supporting plates.

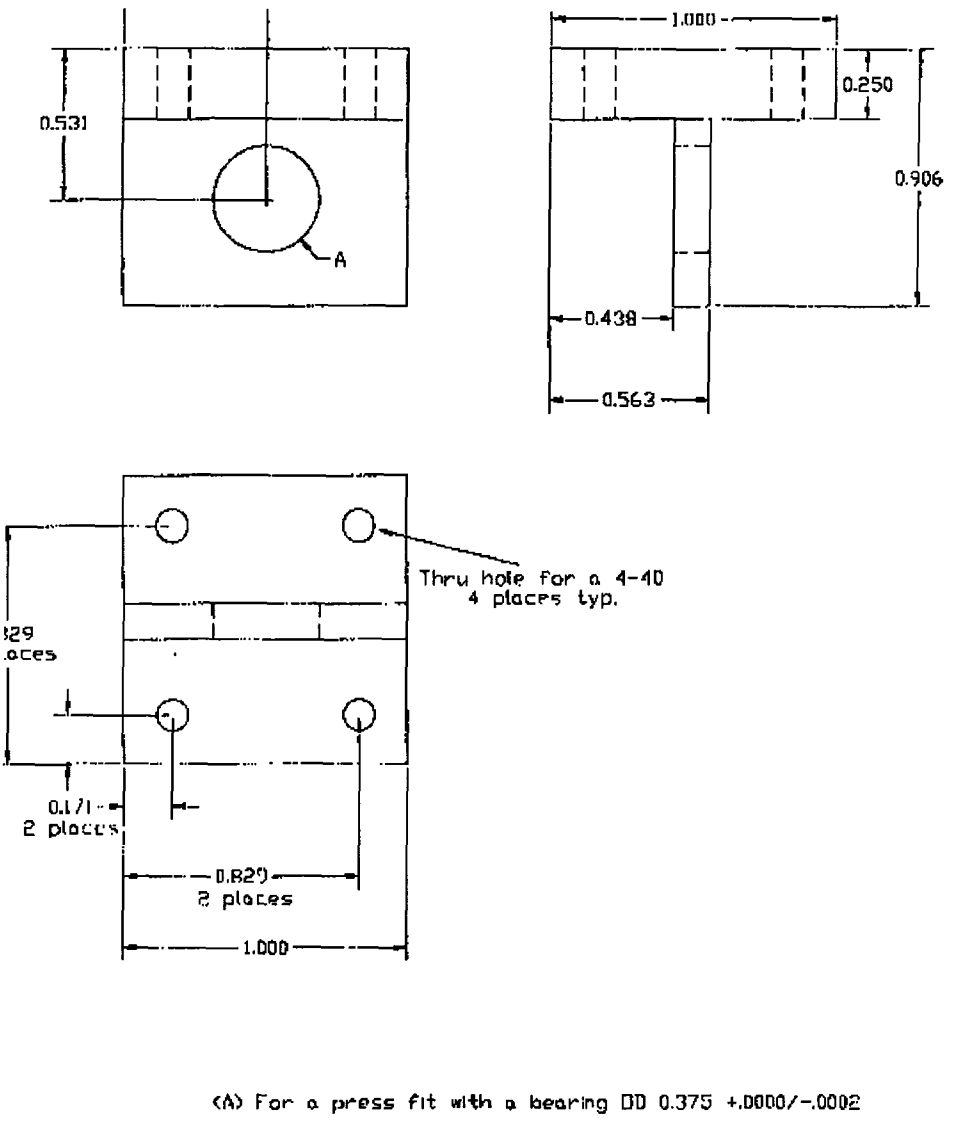

Figure 5.18: The pendulum bearing mount.

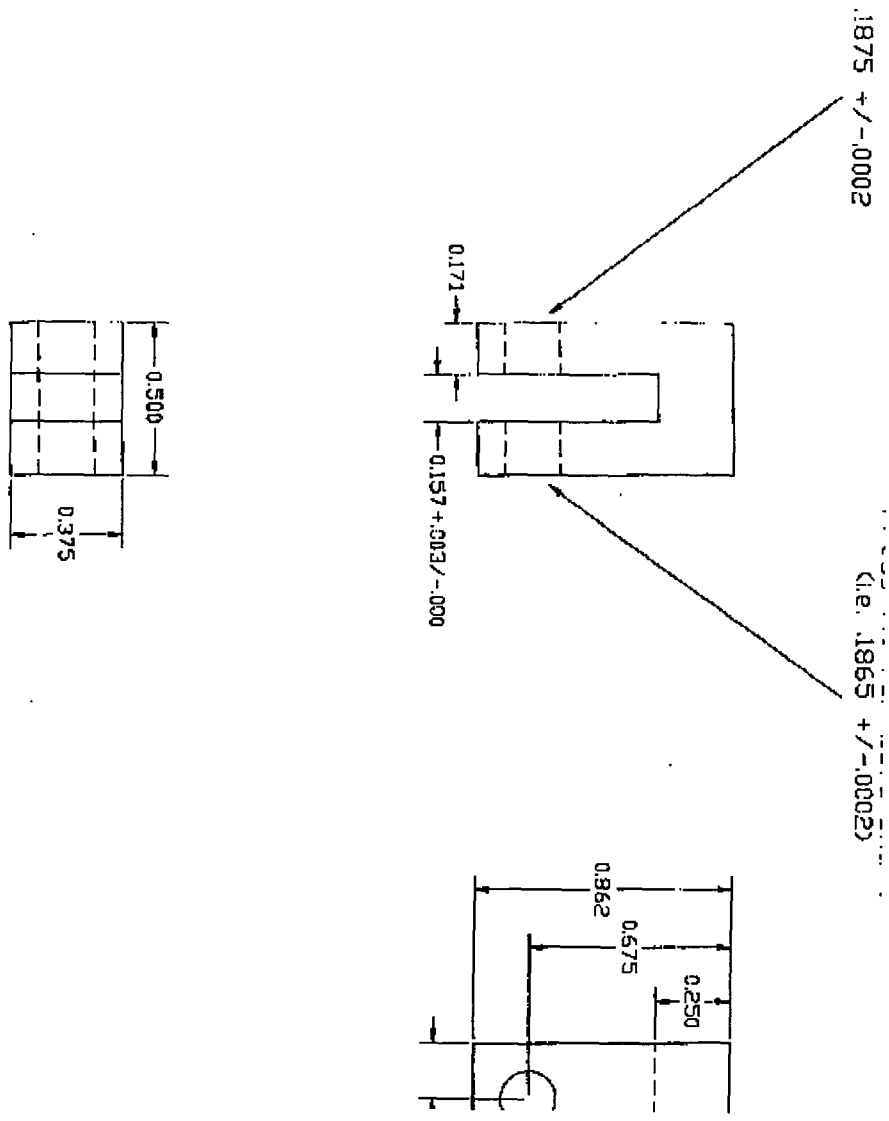

Figure 5.19: The pendulum fork.

5.2.7 Modified Hexagonal head

The base of the magnetostrictive actuator (i.e. the end that does not have the push rod), has a tapped hole into which the positioning differential screw cannot pass through. So a hexagonal head screw with a finely polished head is designed to fit into the hole. The differential screw then pushes against this head.

5.2.8 The Bronze Clamp

The end of the piezoelectric stack facing the disc is glued onto a soft bronze clamp. The choice of the material ensures that it will wear out before the precision machined disc. The clamp itself is separable into two halfs, so that only the lower half needs to be replaced while experimenting with other frictional materials.

5.3 The Lower Half

The main functional component of the lower half is the precision machined disc. The structural components consist of the front and the back bearing plates, the spacer plates and the base plate.

5.3.1 The Disc

The disc is made of stainless steel with an outer diameter of 10 cm, with a tolerance of 2 microns (fig. 5.22). Actually, it is required that the diameter of the disc after press fitting the bearings should have a tolerance of 2 microns. This can be achieved by first coarsely machining the disc, then press fitting the bearings and the bearing plates and finally doing a fine machining.

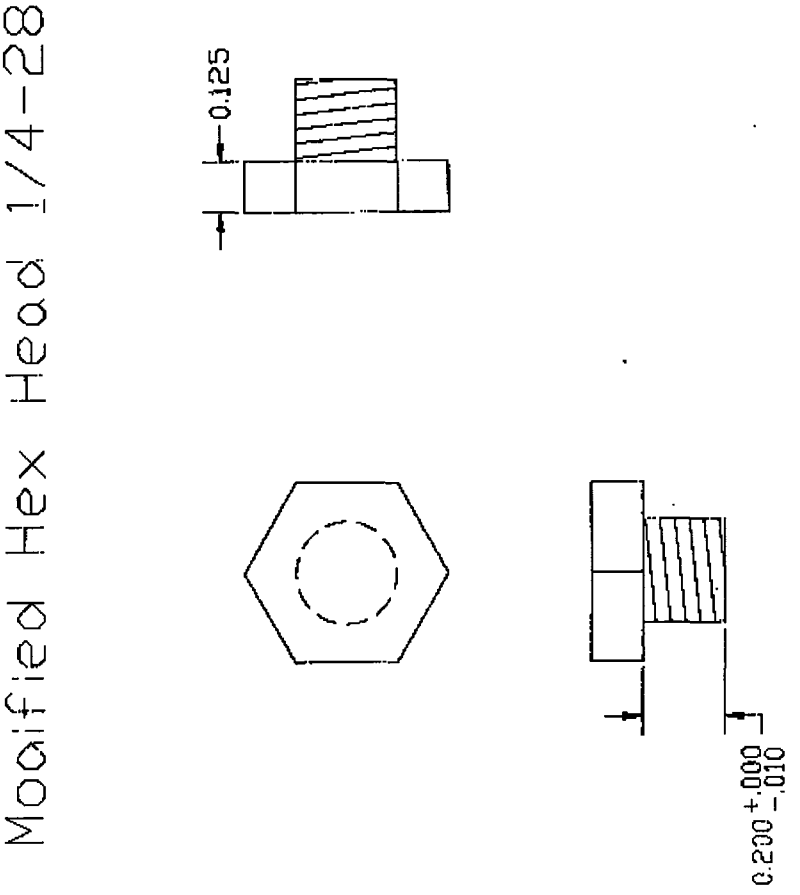

Figure 5.20: The modified hexagonal head.

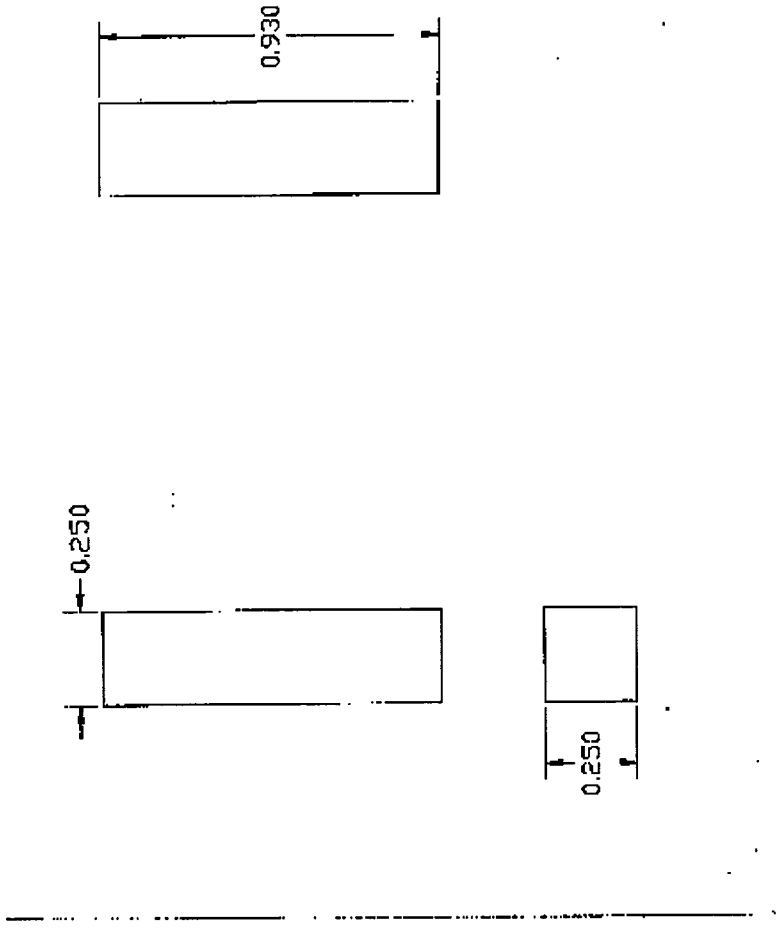

Figure 5.21: The bronze clamp.

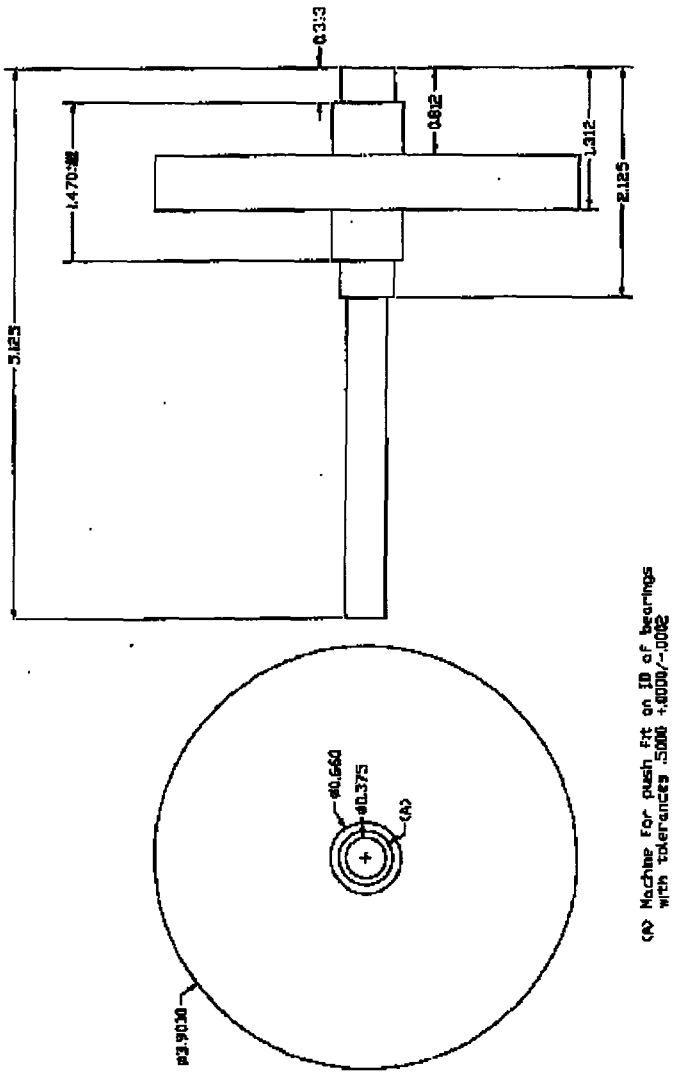

Figure 5.22: The disc.

5.3.2 The bearing plates

The bearings on the disc are mounted on the front and the back bearing plates respectively. The only difference between them is that the back bearing plate has four additional holes for connecting it to the lower connecting bracket of the vertical slide (fig. 5.2). The bearing plates are connected to the base spacer plates (thus completing a rectangle). They are connected to the base plate via dowel pins, so that there is no relative movement between the bearing plates and the base plate.

5.3.3 The Spacer Plates

These are neccessary to keep the distance between the bearing plates within 0.0005 inches (fig. 5.25).

5.3.4 The Base Plate

This forms the bottom of the hybrid actuator assembly. As mentioned in a previous section, the base plate is connected to the bearing plates by dowel pins. It has a hole in the center for measuring the diameter of the disc while fine machining it (fig. 5.26).

Both the halfs of the assembly are held together by the vertical slide (fig. 5.2). The bottom endplate of the slide is connected to the back bearing plate, while the carriage is connected to the back plate of the top half.

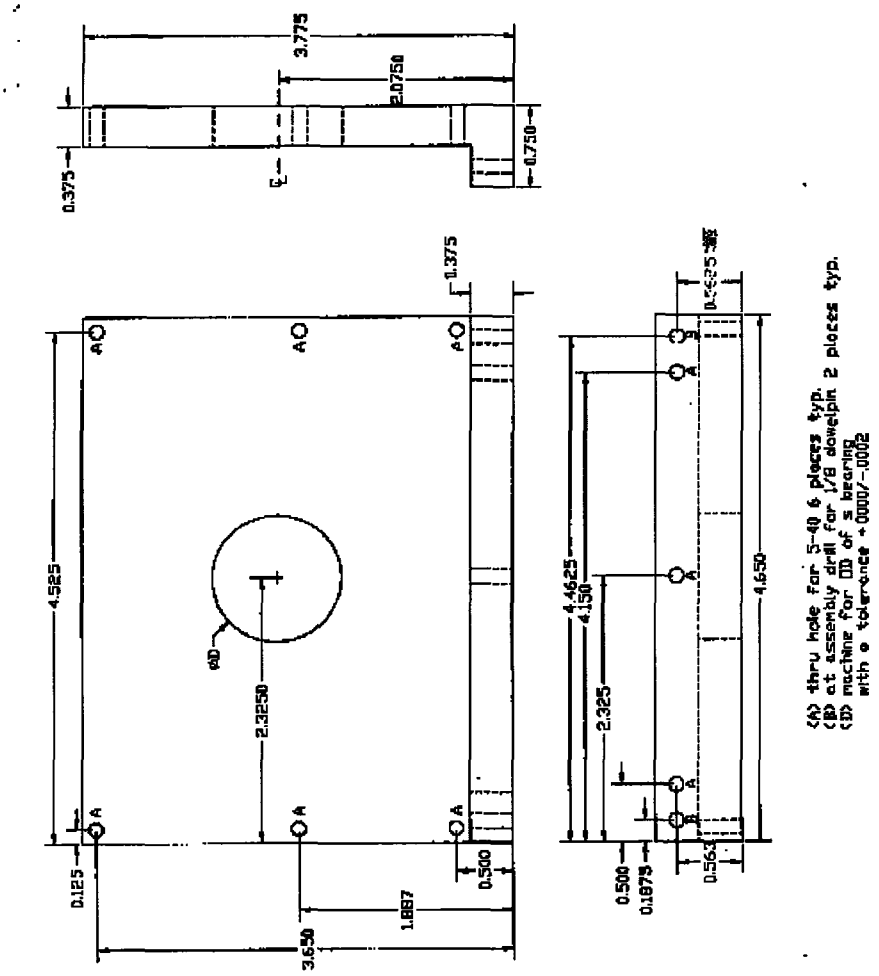

Figure 5.23: The front bearing plate.

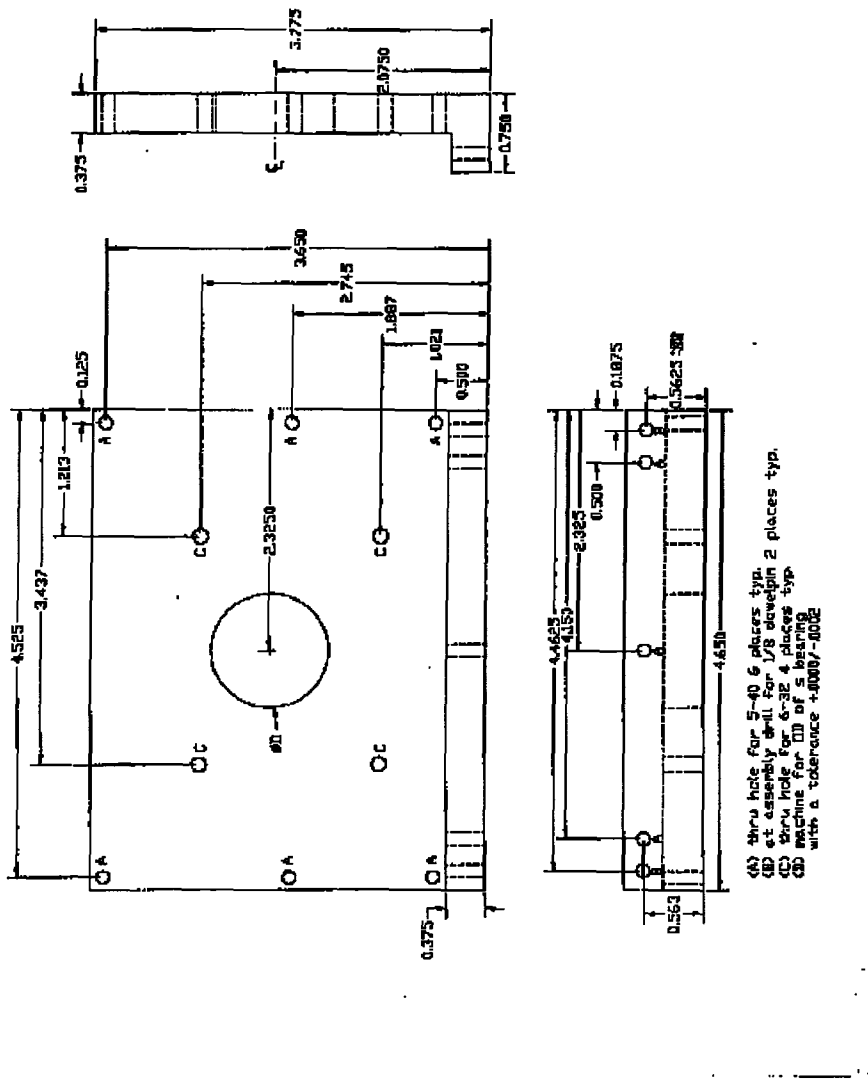

Figure 5.24: The back bearing plate.

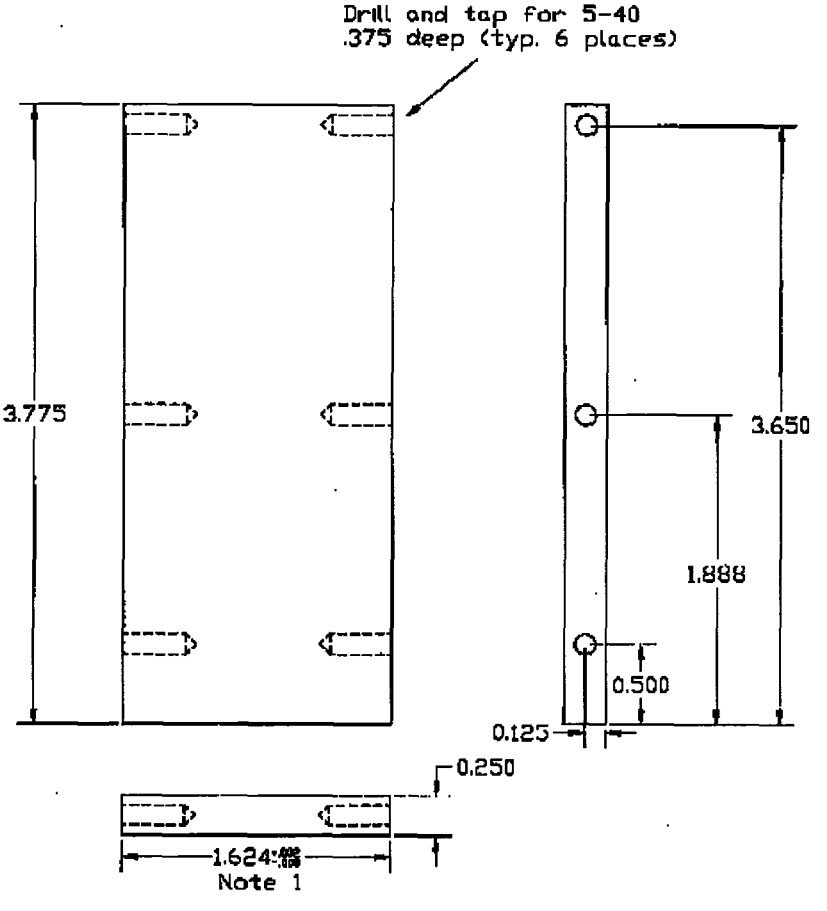

Figure 5.25: The spacer plates.

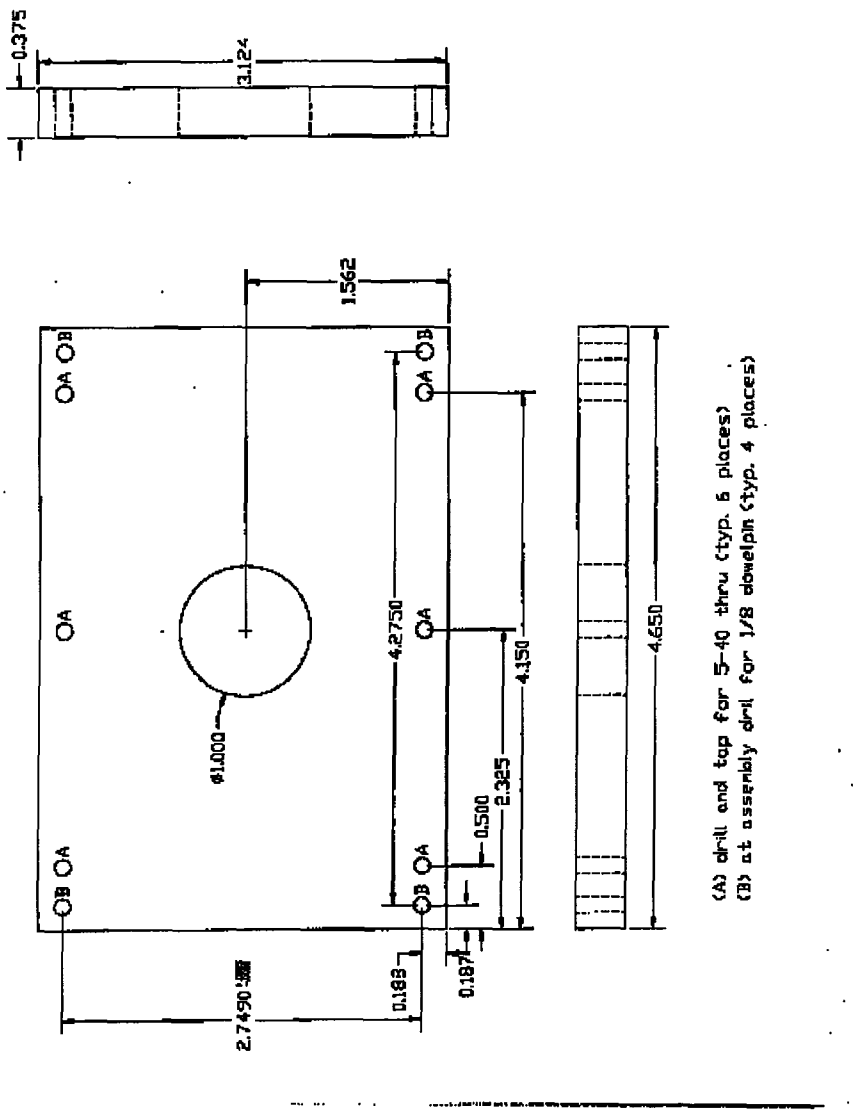

Figure 5.26: The base plate.

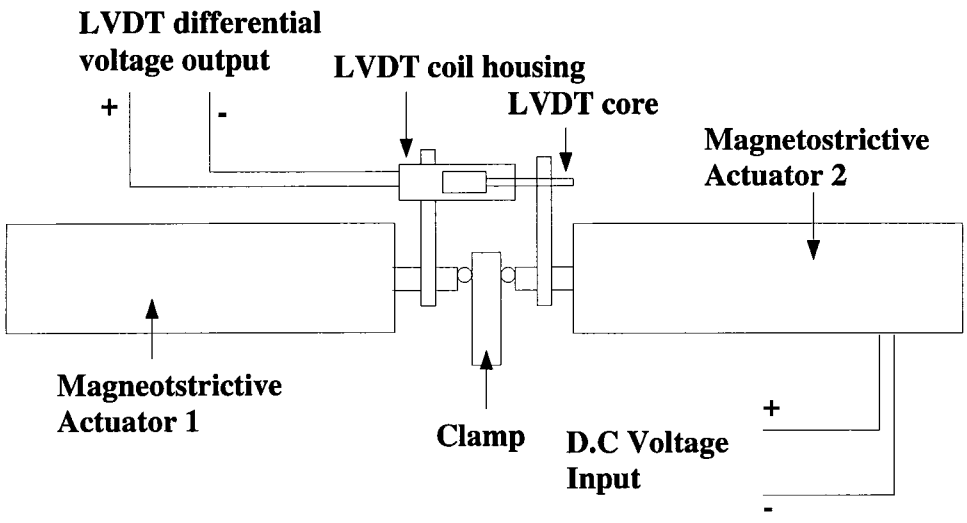

Figure 5.27: Schematic for matching the magnetostrictive actuators.

5.4 Matching The Magnetostrictive Actuators

It is essential to match the magnetostrictive actuators, so that the backward motion of one is equal to the forward motion of the other. This matching can be achieved by either adjusting the prestress or the magnetic biasing field on one of them. Since the prestress is due to Belleville washers which have nonlinear behaviour, it is better and more convenient to adjust the prestress with an external direct current. Now the problem remains to find out just when the matching occurs. This can be done using Linear Variable Differential Transformer (LVDT) sensors (fig. 5.27). With both the coils energized (not shown in the figure), the D.C biasing voltage is increased until the differential voltage output of the LVDT is zero. Once this is accomplished, then the matching appratus is removed, and during regular operation the biasing voltage is applied to the actuator 2.

Chapter 6

Conclusions and Suggestions for Future Work

In this thesis, a novel hybrid motor incorporating both piezoelectric and magnetostrictive actuators has been proposed. A model of this actuator has been developed, taking into account elastic components, friction and impact effects. A computer program has been written to simulate the behaviour of the motor. An example of the use of the motor for helicopter flaperon actuation has been studied. Due to unforeseen delays, even though a prototype motor based on the principle has been built, it has not been tested yet. The testing of the motor will provide proof of concept. The behavior of a series of such actuators can be a direction for future research. Another direction can be the development of a control strategy for precision positioning.

Bibliography

[1] S. Ueha and Y. Tomikawa, *Ultrasonic Motors: Theory and Applications.* Clarendon Press, Oxford, 1993.

[2] Burleigh Instruments, Inc., Burleigh Park, Fishers, NY 14453, *The Micropositioning Book.*

[3] R. Rezaiifar, "Smart structures and wavelet based system identification," Master's thesis, University of Maryland, 1993.

[4] D. Naik and P. DeHoff, "Magnetostrictive direct drive motors," tech. rep., Department of Mechanical Engineering and Engineering Science, University of North Carolina at Charlotte, June 1992. Final Report.

[5] I. Hayashi, N. Iwatsuki, M. Kawai, J. Shibata, and T. Kitagawa, "Development of a piezo-electric cycloid motor," *Japan Society for Precision Engineering*, vol. 57, pp. 1461–1467, August 1991.

[6] C. Walz and I. Chopra, "Design and testing of a helcopter rotor model with smart trailing edge flaps," in *The 35th Dynamics and Materials Conference and Adaptive Structures Forum*, April 1994.

[7] D. Samak and I. Chopra, "A feasibility study to build a smart rotor: Trailing edge flap actuation," in *SPIE International Conference on Active Materials and Adaptive Structures*, February 1993.

[8] C. M. Bothwell, R. Chandra, and I. Chopra, "Torsional actuation with extension-torsion composite coupling and magnetostrictive actuators," in *The 35th Dynamics and Materials Conference and Adaptive Structures Forum*, April 1994.

[9] M. V. Gandhi and B. Thompson, *Smart Materials and Structures.* Chapman and Hall, 1992.

[10] J. L. Butler, *Application Manual for the Design of ETREMA TERFENOL-D Magnetostrictive Tranducers*, 1988.

[11] S.Herman and R. Prodan, "A macroscopic model of eddy currents," in *Eddy-Current Characterization of Materials and Structures* (G. Birnbaum and G. Free, eds.), pp. 86–93, ASTM STP 722, 1981. American Society for Testing and Materials.

[12] K. Uchino, "Ceramic actuators: Principles and applications." MRS Bulletin, April 1993.

[13] E. Flint, C. Liang, and C. A. Rogers, "Electromechanical analysis of piezoelectric stack active member power consumption." Presented at the Smart Structures Symposium, University of Maryland, 1994.

[14] W.Goldsmith, *Impact.* Edward Arnold, London, 1960.

[15] Q.F.Wei, P. Krishnaprasad, and W.P.Dayawansa, "Modeling of impact on a flexible beam," in *Proc. of the 32th Conference on Decision and Control(CDC)*, vol. 2, pp. 1377–1382, 1993.

[16] B. Armstrong-Hélouvry, P. Dupont, and C. C. de Wit, "A survey of models, analysis tools and compensation methods for the control of machines with friction," *Automatica*, vol. 30, no. 7, 1994. Preprint.

[17] P. Dupont and D. Bapna, "Stability of sliding frictional surfaces with varying normal stress." submitted to Applied Mechanics Reviews, August 1992.

[18] Y. Tada, M. Ishikawa, and N. Sagara, "1991 polymer preprints." Japan, 1991.

[19] *Guide to Modern Piezoelectric Ceramics.*

[20] M. Bauccio, ed., *ASM Metals Reference handbook.* Materials Park, OH 44073-0002: ASM International, 1991.

[21] D. Samak and I. Chopra, "Design of high force, high displacement actuators for helicopter rotors," in *SPIE's North American Conference on Smart Structures and Materials*, February 1994.

[22] R. Graf, *The Encyclopedia of Electronic circuits.* Tab Books, Blue Ridge Summit, PA, 1985.